Development of experimental technique for the measurement of refractive index profile for different kinds of conventional and microstructured optical fibers

by

Edgar Saucedo Casas

A Thesis submitted for the degree of

Doctor en Ciencias (Óptica)

Centro de Investigaciones en Óptica, A.C.
León,México

Diciembre 2007

Dedicated to the patience of my parents

"……., Its father is the Sun, Its mother is the Moon,
the wind carried itin its belly,…….".

Hermes Trismegistus (2270 B.C.)

Acknowledgements

I wish to tank to my advisor Dr. Uldazimir P. Minkovich for encourage me to do research in the field of Optical Fibers, for his trust in having allowing me to work in his Laboratory.

I would also want to thank to Dra. Reyna Duarte for her help and collaboration with the optical material corresponding of the Postgraduate Laboratories.

I am also grateful to Lic. Guillermina Muñiz for her attendance in these years.

Thanks to my friends José Trinidad Guillen, Luis CarlosAlvarez and J.L. Cabellos for shearing their friendship, it had a great value.

"*All the small ones, the trivial things or insignificant things are good to complete the splendor of the infinitum".*

Giordano Bruno Nolano.
Of the Infinite Universe and Worlds (1584)

Contents

List of Figures

2.12 (b**)** Scheme of an equivalent simple microscope. S represents the light source, O is the tested object, L_1 is the objective, L_2 is the ocular, ***I*** stands for the focused image in the plane B, and the defocused images are taken by ΔF.

2.13 A defocused red blood cell.

3.1 Schematic diagram showing (a) end view of the fiber and (b) transverse view.

3.2 Scheme of the Experimental Setup of the optical system.

3.3 Experimental Setup.

3.4 Tested optical fibers pieces are placed between silica covers.

3.5 Experimental bright field microscopic image of (a) Corning 62.5/125 graded index fiber, (b) 60/125 nearly step-index fiber, and (c) doped ytterbium-holmium fiber.

3.6 (a) Transverse phase gradient image of the Corning 62.5/125 graded index fiber and (b) Averaged transverse phase gradient image of the optical fiber.

3.7 (a) Transverse phase gradient image of the 60/125 conventional step-index fiber and (b) Averaged transverse phase gradient image of the optical fiber.

3.8 (a) Transverse phase gradient image of the heavily doped ytterbium-holmium silica fiber and (b) Averaged transverse phase gradient image of the optical fiber.

3.9 Refractive index profiles of the Corning 62.5/125 optical fiber.

3.10 Refractive index profile of the 60/125 conventional step-index optical fiber.

3.11 Refractive index profile of the heavily doped ytterbium-holmium silica optical fiber obtained in experiments.

3.12 Image of faulty pinhole.

3.13 Unreliable experimental bright field microscopic image of Corning 62.5/125 graded index fiber.

4.1 Schematic diagram of MOF showing (a) end view and (b) transverse view.

4.2 Microscope slide where the fiber pieces are placed between silica covers.

4.3 Conventional Corning 60/125 step-index fiber images obtained with DC3-163 video-microscope at white light illumination: (a) end view of the fiber, (b) transverse view.

4.4 Images of Corning 60/125 step-index fiber: (a) experimental bright field microscopic image, (b) transverse phase gradient image, (c) averaged transverse phase gradient image.

4.5 Refractive index profile of the 60/125 conventional step-index fiber.

4.6 Experimental MOF with two dimensional cladding: (a) end view of the fiber, (b) transverse view. Outer diameter of the fiber is 125 μm, diameter of the core 15.6 μm, and relative hole diameter $d/\Lambda = 0.42$.

4.7 Experimental large-mode-area MOF: (a) end view of the fiber, (b) transverse view. Outer diameter of the fiber is 125 μm, diameter of the core is 11.6 μm, and the relative hole diameter of the cladding $d/\Lambda=0.5$.

4.8 Bright field microscopic images: (a) experimental MOF with two dimensional cladding and the relative hole diameter of the inside cladding $d/\Lambda=0.42$; (b) experimental large-mode-area MOF with $d/\Lambda=0.5$.

4.9 Experimental setup used for tested experimental MOFs.

4.10 Experimental MOF with two dimensional cladding: (a) transverse phase gradient image, (b) grey scale integer values of the phase gradient image.

4.11 Large-mode -area MOF with $d/\Lambda=0.5$: (a) transverse phase gradient image, (b) grey scale integer values of the phase image.

4.12 Averaged index profile for experimental MOF with two–dimensional cladding and with relative hole diameter of inside cladding $d/\Lambda=0.42$.

4.13 Averaged index profile for large-mode area MOF with $d/\Lambda=0.5$.

5.1 Focus bright field microscopic images of (a) Corning 62.5/125 graded-index fiber, (b) 60/125 step-index fiber, and (c) 218/227 nearly step-index fiber.

5.2 (a) Defocused transfer function of Corning 62.5/125 graded-index fiber and (b) theoretical bright field microscopic image of the same fiber in the frequency domain.

5.3 (a) Defocused transfer function of 60/125 step index fiber and (b) bright field microscopic image of the same fiber in the discrete frequency domain.

5.4 (a) Defocused transfer function of 218/227 step index fiber and (b) bright field microscopic image of the same fiber in the discrete frequency domain.

5.5 Dashed and solid curve show, respectively, the refractive index profile of the same Corning 62.5/125 graded-index fiber obtained with common procedure and with the optical transfer function.

5.6 Dashed curve shows the refractive index profile of 60/125 step-index fiber obtained with common procedure. Solid curve is the refractive index profile of the same fiber at using the optical transfer function.

5.7 Solid and dashed curves show, respectively, the refractive index profiles of the same 218/227 nearly step-index fiber obtained with common procedure and with the optical transfer function.

A. Reference system for a traveling wave.

Chapter 1

Introduction

1.1 Background

Many optical investigations require of laser sources as well as waveguide schemes, Besides in the last years together with the development of optical fibers, which are able to transfer electromagnetic fields over hundreds of kilometers become an important tool in the new period of time for worldwide high speed telecommunication systems. So, many forms of communications procedures have appeared over the most recent years. The principal motivations behind each new one were either to make better the transmission fidelity, to improve the data rate so that more information could be sent, or to increase the transmission distance [1]. In the most recent years, the speed or bandwidth at which a single optical fiber could send data seemed pretty much unlimited. Step by step the bandwidth of telecommunication networks became too small, but it seemed that the limitation was not so much due to the inherent limits of the waveguide, but much more to the limited speed of the signal sources and receivers. Investigations for increasing the bandwidth of optical networks in these days is more a question of how to get the best out of fibers through injecting more information, than a question of improving optical waveguides.

We have seen recently that, with the increasing demand for bandwidth, basically due to the popularization of the worldwide telecommunication networks and multimedia contents, along with the progress made in high speed electronics and optoelectronics, the inherent

limits of optical fibers were reached. In addition to telecommunication applications [2], optical fiber links have been installed in not antiquated electrical power plants. These links are used to transmit information for system protection, supervision, and control, which are extremely important in large and complex modern power plants. In this manner, the immunity of optical fibers to inductive interference and their high data transmission capacity thus offer an excellent possibility to telecommunication systems.

Nowadays, higher density data injection is possible, but because of non-linear effects of new microstructured composition in the optical fibers (they are called microstructured optical fibers MOFs), where in many cases they have been done by arranging a collection of tubes around a solid central rod. A basic scheme of this structure can be seen in Figure 2.4. Thus, other effects which can be developed in the field of optical fiber technology, which is constantly undergoing changes and improvements.

The discovery of these new microstructured optical fibers MOFs (In the early 1990s), they showed that they could have unprecedented properties and overcome many limitations intrinsic to conventional optical fibers. The possibilities of microstructured optical fibers brought prospects of totally new fields of application for fiber optics, such as optical fibers for high power applications [1], optical fibers for non-conventional wavelengths ranges like far infrared and ultra violet regimes, compact high precision metrology and innovative optical fiber sensors (OFS) [2], Here, we can enumerate some general advantages of OFS, properties like: immunity to the electromagnetic interference, .lightweight, small size, high sensitivity and large bandwidth. In addition, these optical sensors have the versatility of being configured in arbitrary shapes specially in new geometrical configurations in the field of new microstructured optical fibers and in this manner they offer a technological base in the scheme to sensing more diverse physical quantities, just as: temperature, pressure, rotation, thermal conductivity, voltage and so on.

On the other side, we can say that one of the main properties of solid core in MOFs discovered is that they can be single-mode over an infinite range of wavelengths [3], this essential attribute becomes an important property over all conventional optical fibers, and it gives the possibility of manipulating high power electromagnetic fields regimes. Then, such microstructured fibers are a topic of active research worldwide because of their potential significance in the development of novel optoelectronic and photonics devices. Also, MOFs with different planar geometries are studied and developed for novel ways to manipulate the flow of light and at the same time they have shown great capability for many applications in the field of optics, as we have said before [4].

In all kind of optical waveguides (conventional and micostructured optical fibers) the knowledge of the main physical properties of these fibers keeps being the principal objective for improving the fibers properties in the plane of optical fiber technology and telecommunication applications [5].

To a large extent, the studies of the physical properties in optical fibers have been playing an important role during their manufacturing process. In this sense, if we are talking about the refractive index function of the optical fibers is considered indeed one of the most important parameter in the optical fibers area: Thus, the main motivation coming because through refractive index profile can be determined various physical attributives on the optical fibers, such as: mode file profiles, dispersion characteristics, power transmission coefficients optical power carried by modes and so on.

1.2 Opto-measurement systems

Up to these years, there are several numbers of techniques where refractive index function is obtained with a good approximation [4]. Alone to mention one of them, a well-known "Imaging Optometronic System" [6], which has recently been applied for testing and

studying multiple types of waveguides, arrayed waveguides and other photonic circuits. This mentioned system operates with a conventional optical microscopy system simultaneously with an atomic force microscopy, which has the additional advantage of allowing for extremely precise optical fiber control and movement. A basic scheme of the previously described system is drawn in the Figure 1.1

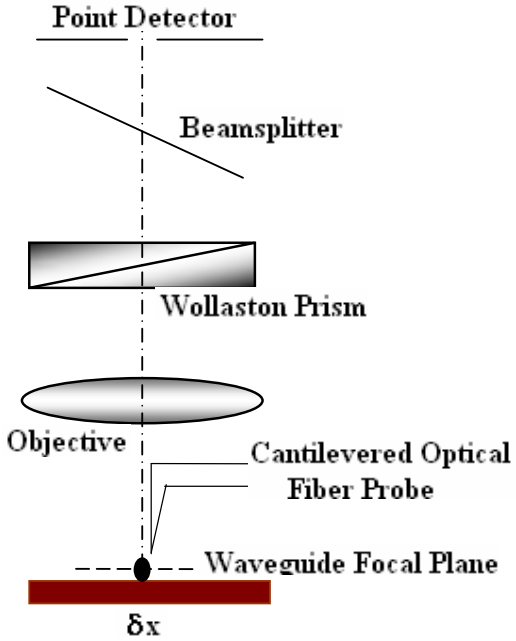

Figure 1.1 Wollaston Prism splitting rays of light into two beams with a separation δx in the Optometronic system.

The above described system contains a Wollaston prism that can split the rays of the laser beam into two beams with a separation δx, these two beams can follow a different optical path which is detected on the Point detector. Thus, the physical information is obtained for this difference of optical path.

Then, among all different techniques, non-destructive methods are more usually spread because they are able to get physical information from the system without modify the system, and beside we can apply inside them image processing tools, where it is well known that image processing is an extensive set of functions for processing multidimensional arrays, at

which they can be satisfactory used in the field of optical fibers qualities. Thus physical properties can be achieved by meaning of numerical procedures over these arrays.

In the content of the present dissertation, axially symmetry is introduced as a main feature of the studied optical fibers, which provides an important role when we estimate final results. Also, we describe the experimental results, with the purpose of having a particular refractive index profile in each particular fiber specimen and consequently the experimental difficulties and sources of errors are discussed, all this with the purpose of getting a better estimation of refractive index profile function.

In this dissertation is described a method of obtaining refractive index function using a basic experimental arrangement which it works with a well-determined wavelength monochromatic source illumination and thus finally visual fields have been taken by a microscopy system. Several examples of optical fibers have been tested, and the application of the method to measurement the refractive index profile is also discussed in general form. All these techniques are described for static systems where the environmental conditions are almost supposed under control in the laboratory, but we hope all these measurement techniques could be applied to the industry where the environmental conditions are usually harder tested for the optical devices and where it requires a better precision and maybe several different numerical procedures.

1.3 Contents by Chapter.

The thesis contains five chapters, the first and second Chapters are addressed to Introduction and Basic concepts of Conventional and Microstructured Optical Fibers (MOFs). The study and application of a non-destructive and non-interferometric method based on bright field microscopy images for conventional optical fibers is treated in Chapter 3, and for large-mode-area MOFs in the Chapter 4.

In Chapter 5, a defocused transfer function of experimental bright field microscopic images are applied together with the simple experimental technique for the measurement of refractive index function of conventional optical fibers.

References

[1] G. Keiser, *Optical Fiber Communications*, Student Ed.(McGraw-Hill, 1984).

[2] J.I. Kim, *Analysis and Applications of Microstructured and Holey Optical Fibers,* Ph. D. Thesis (Virginia Polytechnic Institute, 2003).

[3] T.A Birks, J.C. Knight, and P. St. J. Russell, "Endlessly single-mode photonic crystal fiber", *Opt. Lett.* Vol.22, pp.961-963 (1997).

[4] A. Bjarklev, J.Broeg, A. Sanchez Bjarklev, *Photonic Crystal Fibers,* (Kluwer Academic Publishers, 2003).

[5] K. Okamoto, *Fundamentals Optical Waveguides* (Academic Press, 2006).

[6] *Imaging at nanoscale,* http:// www.nanonics.co.il/refractive-index-profiling.htlm

Chapter 2

Basic Concepts of Optical Waveguides and the transport-of intensity equation.

2.1 Optical Waveguides

A conventional optical fiber is composed of a cladding usually made of silica and a core of doped silica (in general cases with germanium). The refractive index function of the silica cladding n_2 is subsequently only just smaller than the refractive index function of the core n_1. Generally, the refractive index difference between core and cladding is of the order of $n_1 - n_2 = 0.01$. Therefore the electromagnetic field that is coupled to the end face of the waveguide is partly reflected and partly refracted at the core-cladding interface. The angle of incidence of the electromagnetic field and the angle of refracted field are related according to the Snell´s Law

$$n_1 \sin\theta_1 = n_2 \sin\theta_2$$

Here, θ_1 and θ_2 are the incident and refracted angle with respect to the normal to the core-cladding interface as it is shown in the following Figure 2.1

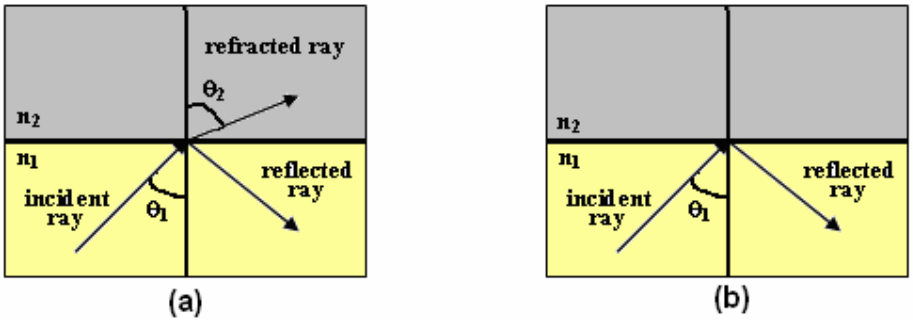

Figure 2.1 Schematic representation of (a) refracted and reflected beams and (b) total internal reflection beam

According to Snell´s law, the function $\sin(\theta_2)$ has a limit value ***1***, and if

$\theta_1 = arcsin\left(\frac{n_2}{n_1}\right)$, then when the condition $\theta_1 \geq arcsin\left(\frac{n_2}{n_1}\right)$ is fulfilled, the

electromagnetic fields are fully reflected at the core-cladding interface and they

propagate inside the core of the fiber. A basic structure and refractive index profile of the optical waveguides are shown

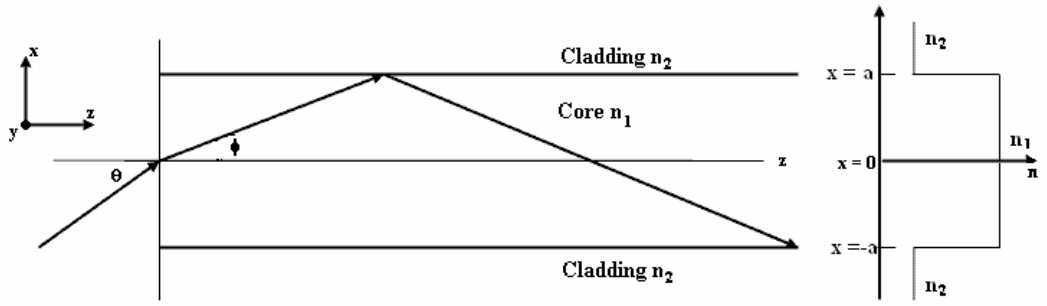

(a)

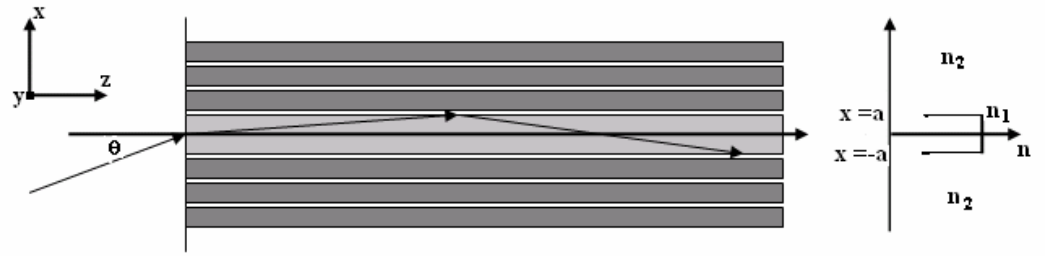

(b)

Figure 2.2 (a) Total internal reflection in conventional fiber and (b) in microstructured optical fiber (MOF).

The transmission properties of an optical waveguide are dictated by its structural characteristics, which have a principal effect in determining how an optical signal is affected as it propagates along the fiber. Let us consider a plane waves propagating along the z-direction with inclination angle ϕ, the plane waves are perpendicular to the light rays, in addition, the wavelength and the wave number of the electromagnetic fields in the core are λ/n_1 and kn_1 (where $k=2\pi/\lambda$), respectively, here the wavelength λ is given in vacuum space. The propagation constants along *z* and *x* (lateral direction) are represented by [1]:

$$\beta = kn_1 \cos\phi \qquad \text{and} \qquad \kappa = kn_2 \sin\phi,$$

And then, the propagation of electromagnetic fields along a waveguide can be described in terms of a set of guided electromagnetic waves called the “modes” of the waveguide. These guided modes are referred to as the bound modes of the waveguide. In this manner, each guided mode is a patter of electric and magnetic field lines that is repeated along the fiber at intervals equals to the wavelength. Only a certain discrete number of modes are capable of propagating along the waveguide. These modes are those electromagnetic waves that satisfy the homogeneous wave equation in the waveguide and the boundary conditions at the core-cladding interface.

Thus, Maxwell`s equations determine the spatial dependence of the electrical field **E**(x,y,z) and the magnetic field **H**(x,y,z) in an optical waveguide. It has been assumed an implicit time dependence $exp(-iwt)$ for both field vectors. The dielectric constant ε(x,y,z) is related with the refractive index function n(x,y,z) by $\varepsilon=n^2\varepsilon_0$, where ε_0 is the permittivity value in the vacuum space. Besides, for nonmagnetic materials which usually constitute an optical waveguide, the magnetic permeability of the medium μ is almost always equal to the vacuum space value μ_0.Then, Maxwell`s equations in a homogeneous and lossless dielectric medium are written in the form [2]:

$$\nabla \times \mathbf{E} = i\sqrt{\frac{\mu_0}{\varepsilon_0}}k\mathbf{H} \qquad \nabla \times \mathbf{H} = -i\sqrt{\frac{\mu_0}{\varepsilon_0}}kn^2\mathbf{E} \qquad (2.1)$$

$$\nabla \bullet \mathbf{E} = 0 \qquad \nabla \bullet \mathbf{H} = \mathbf{0}$$

Here, the free-space wavelength number stands for k and λ is the wavelength of the light in the vacuum. Strictly speaking, in a waveguide, we have a two-dimensional refractive index function $n=n$(x,y), where in this situation the waveguide become translationally invariant. Therefore the modal field vectors can be expressed by:

$$\mathbf{E}^j(x,y,z) = (\mathbf{E}_\perp^j(x,y) + E_z^j\hat{\mathbf{e}}_z)\exp(i\beta^j z)$$
$$\mathbf{H}^j(x,y,z) = (\mathbf{H}_\perp^j(x,y) + H_z^j\hat{\mathbf{e}}_z)\exp(i\beta^j z) \quad (2.2)$$

β^j is the propagation constant of the *j*-th mode. Here, $\mathbf{E}_\perp^j = E_x^j\hat{\mathbf{e}}_\mathbf{x} + E_y^j\hat{\mathbf{e}}_\mathbf{y}$;

$\mathbf{H}_\perp^j = H_x^j\hat{\mathbf{e}}_\mathbf{x} + H_y^j\hat{\mathbf{e}}_\mathbf{y}$, Here, E_z^j and H_z^j are the transverse and longitudinal components of the modal electric and magnetic fields, respectively.

In the case of cylindrical polar coordinates the field vectors are:

$$\tilde{\mathbf{E}}(r,\phi,z) = \mathbf{E}(r,\phi)\exp(i\beta z) \quad \tilde{\mathbf{H}}(r,\phi,z) = \mathbf{H}(r,\phi)\exp(i\beta z) \quad (2.3)$$

Replacing the equations (2.2) into (2.1) and comparing the field components the following expressions are obtained [2]:

$$\mathbf{E}_\perp = \sqrt{\frac{\mu_0}{\varepsilon_0}}\frac{1}{kn^2}\{\beta\mathbf{H}_\perp + i\nabla_\perp H_z\}\times\hat{\mathbf{e}}_z$$
$$E_z = i\sqrt{\frac{\mu_0}{\varepsilon_0}}\frac{1}{kn^2}\hat{\mathbf{e}}_z\bullet(\nabla_\perp\times\mathbf{H}_\perp)$$
$$\mathbf{H}_\perp = \sqrt{\frac{\varepsilon_0}{\mu_0}}\frac{1}{k}\hat{\mathbf{e}}_z\times\{\beta\mathbf{E}_\perp + i\nabla_\perp E_z\} \quad (2.4)$$
$$H_z = -i\sqrt{\frac{\varepsilon_0}{\mu_0}}\frac{1}{k}\hat{\mathbf{e}}_z\bullet(\nabla_\perp\times\mathbf{E}_\perp)$$

Here, operator $\nabla_\perp$ represents transverse gradient and the two-dimensional refractive index function is written by $n=n(x; y)$ and the wavelength number k.

In both cases, conventional and microstructued optical fibers (MOFs), the number and characteristics of these electromagnetic fields depend on the fiber parameters (refractive

index function, core size, and in the special MOFs case, where their cross-section is a web on m-hexagonal rings of air-holes).

Maxwell´s Equations (2.4) do not determine the electromagnetic fields in optical fibers completely. Out of the endless possibilities of solutions of Maxwell´s equations, we need to take those that satisfy the boundary conditions of each particular fiber. In the majority of the cases the boundary conditions occurs when there are discontinuities in the refractive index function. At the boundary the tangential components of electromagnetic fields should satisfy the conditions of continuity.

2.2 The method of localized basis functions

In the special context of MOFs, It becomes complicated to locate such core-cladding boundaries. Therefore, advanced numerical methods are used for highly accurate modeling of the MOFs. To mention one very well-known, the method of localized basis functions [3], this method is based on the direct solutions of Maxwell`s equations, using a representation of the refractive index function and the electromagnetic field distributions as a sum of localized basis functions. A shortly review of this method is presented right away.

Using the scalar wave equation for the modal electric field $E_x = E_y = E(x, y)$ we have the following mathematical expression:

$$\frac{1}{k^2}\nabla^2 E + n^2 E = \frac{\beta^2}{k^2} E \qquad (2.5)$$

Thus, the localized orthonormal set of Hermite–Gaussian basis function in the XY plane is written as:

$$\psi_a(x)\psi_b(y) = \frac{2^{-a-b}\pi^{-1/2}}{\sqrt{(2a)!(2b)!}\Lambda} exp\left[\frac{-(x^2+y^2)}{2\Lambda^2}\right] H_{2a}\left(\frac{x}{\Lambda}\right) H_{2b}\left(\frac{y}{\Lambda}\right).. \quad (2.6)$$

Here H_{2n} is the 2n-order Hermite polynomial, where only even order polynomials are used, this happens because fundamental mode profiles in MOFs are even. Constant "Λ" is known as pitch of the web and here it takes an important roll. This separable orthonormal functions set keeps the following rules:

$$\begin{aligned} \delta_{ca} &= \int_{-\infty}^{+\infty} \psi_a(x)\psi_b(x)dx \\ \delta_{db} &= \int_{-\infty}^{+\infty} \psi_d(y)\psi_b(y)dy \end{aligned} \quad (2.7)$$

$$\begin{aligned} \frac{d\psi_a(x)}{dx} &= \frac{\sqrt{a}}{\Lambda}\psi_{a-1/2}(x) - \frac{\sqrt{a+1/2}}{\Lambda}\psi_{a+1/2}(x) \\ \frac{d\psi_b(y)}{dy} &= \frac{\sqrt{b}}{\Lambda}\psi_{b-1/2}(y) - \frac{\sqrt{b+1/2}}{\Lambda}\psi_{b+1/2}(y) \end{aligned} \quad (2.8)$$

Let us suppose that, the scalar modal electric field E^m is expanded as:

$$E^m(x,y) = \sum_{a,b=0}^{F-1} \varepsilon_{ab}\psi_a^m(x)\psi_b^m(y) \quad (2.9)$$

At this point, *F* is the number of terms preserve in the expansion. Substituting Eq.(2.9) in (2.5) and then each term is multiplied by $\psi_c(x)\psi_d(y)$ followed by an integration over the transverse plane XY. Making use of expression (2.7) and (2.8) of the complete

Hermite-Gaussian basis functions, after that, an eigenvalue equation is obtained and it is expressed as:

$$\left(\frac{1}{k^2\Lambda^2}\mathbf{A} + n^2\mathbf{I}\right)\hat{\mathbf{v}} = \frac{\beta^2}{k^2}\hat{\mathbf{v}} \tag{2.10}$$

A, I are $(F\text{-}1)^2 x (F\text{-}1)^2$ matrices and the eigenvector $\hat{\mathbf{v}}$ is represented of the subsequent form: $\hat{\mathbf{v}}^T = \left[\varepsilon_{00} \ldots \varepsilon_{0F}\varepsilon_{1F} \ldots\ldots \varepsilon_{FF}\right]$, Here, $\varepsilon_{i,j}$ are the modal fields components.

In the case of particular MOFs (Holey Fibers) [4] the squared index distribution is expanded in two parts, the central index core is represented using the localized Hermite-Gaussian functions defined above, and the periodic lattice of holes is represented using periodic functions (See Figure 2.3). Afterwards, solving the eigenvalue equation (2.10) at specific wavelength λ, the modal field components and the propagation constants of the fiber can be calculated.

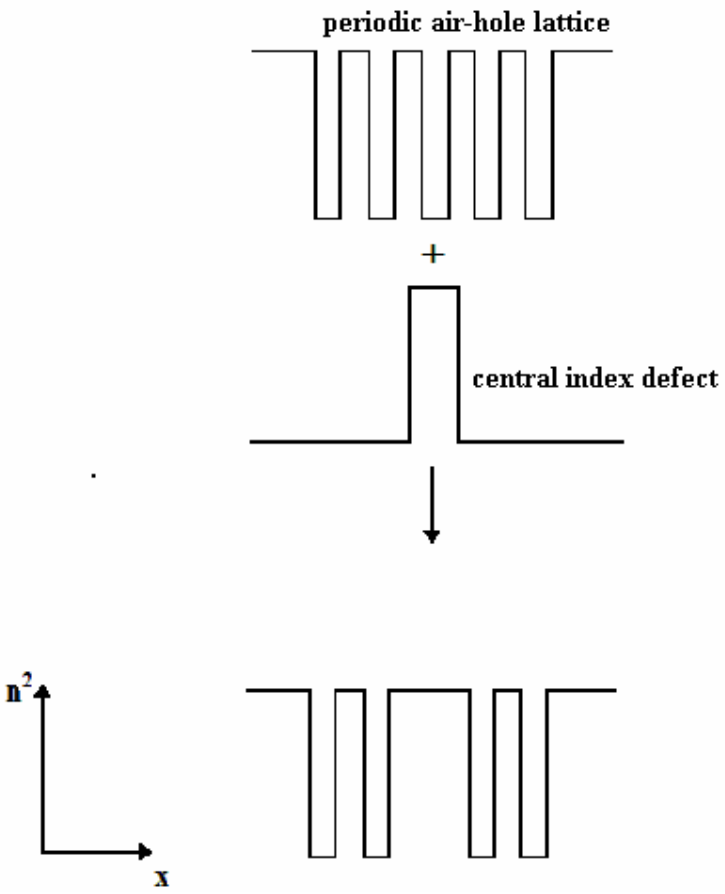

Figure 2.3 Decomposition of squared refractive index profile, A cross section along the *x*-direction is shown

2.3 Classes of Microestructured Optical Fibers.

MOFs can be classified by the dimensions of the fiber structures, and their specific properties. In the case of the total internal reflection principle, three subclasses have today appeared, and they are: High-numerical aperture (HNA) fibers having a wide central core surrounded by a ring of relatively large air-holes, High-Non.Linear (HNL) fibers, having a very small core dimensions to provide tight mode confinement, and finally, Large-Mode-Area fibers, using relatively large dimensions and small effective

refractive index contrasts to spread out the transverse optical field. The set of the all above MOFs are called Holey Fibers.(HF) (See these fibers in Figure 2.4)

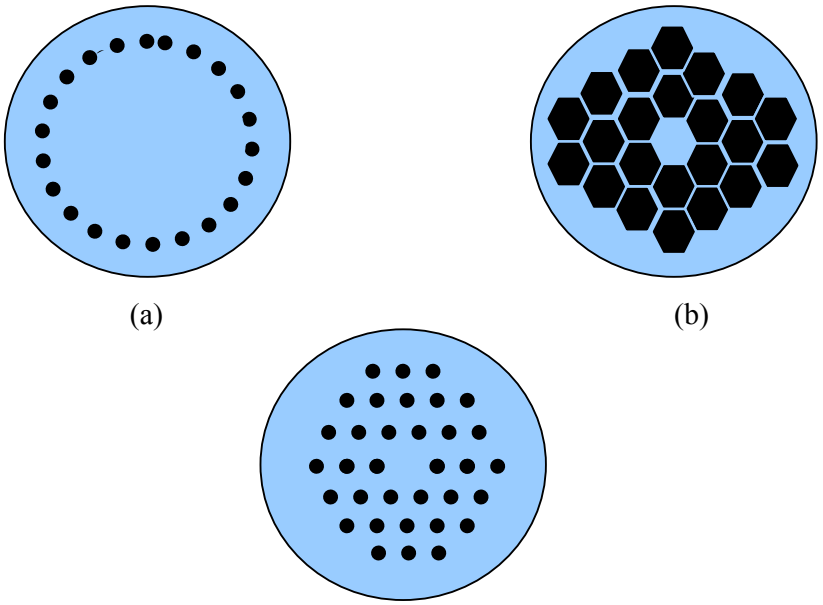

Figure 2.4- Main classes of different Holey Fibers (HF), (a) High numerical aperture fiber (HNA), (b) Highly Non-Linear Fiber (HNL) and (c) Large-Mode -Area Fiber (LMA).

The development of Large-Mode-Area MOFs fibers, whose cross section is a web of m_r hexagonal rings of air-holes of the diameter "d" pitched by the distance "Λ", is very important for a wide range of useful applications most notably those demanding the transmission of high power optical beams. For this large number of applications, spatial mode quality is also a crucial issue, and so, (LMA) fibers should preferably maintain just a single transverse mode.

2.4 Large-mode-area MOFs (Characteristics and Fabrication)

It is well known, that, the intrinsic material absorption of pure silica for wavelengths between approximately 0.6 μm and 1.8 μm is very small, and in the theory light in the wavelength range could be carried hundreds of kilometers almost without any losses, Nevertheless, to compensate for losses, signal amplifiers and repeaters are introduced at intervals, In this sense, the single-mode properties of LMA-MOFs, depend on a very small effective-index contrast between core and cladding, here it is noticed too, that Large-Mode-Area (MOFs) technology provides more accurate direction to controlling the aforementioned index difference between core and cladding regions of the fiber, since the supervision of hole size "*d* " and centre-to centre spacing " Λ" may be used to adjust the exact effective indices. Typically diameter air-hole " *d* " is in the range from 1.1 μm to 3.6 μm and spacing Λ kept fixed, about 6.0-7.5 μm. Thus, the relative hole diameter d/Λ for LMA fibers covers the interval running from 0.14 to 0.6.[5,6]

Returning back with the cross section of the LMA-MOF (see Figure 2.5):

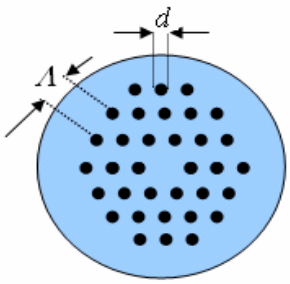

Figure 2.5- Large –Mode-Area Fiber where the air channels have diameter *d* and pitched by distance Λ.

According to reference [8] the geometrical air-filling fraction in a cross-section of a LMA fiber can be expressed by:

$$f_{air} = \frac{\pi}{2\sqrt{3}}\left(\frac{d}{\Lambda}\right)^2 \tag{2.11}$$

Then, the corresponding silicon fraction is:

$$f_{Si} = 1 - f_{air} = 1 - \frac{\pi}{2\sqrt{3}}\left(\frac{d}{\Lambda}\right)^2 \tag{2.12}$$

Therefore, the effective index refraction n_{eff} of the cladding becomes strongly wavelength-dependent of this air-filling fraction. And the following limits should be satisfied the following mathematical expressions:

$$\begin{aligned} &\lim_{\lambda << \Lambda} n_{eff} = n_{Si} \\ &\lim_{\lambda >> \Lambda} n_{eff} = f_{air} n_{air} + (1 - f_{air}) n_{Si} \end{aligned} \tag{2.13}$$

Thus, the above statements give us the possibility of change the refractive index difference between core and cladding by adjusting the relative hole diameter d/Λ.

In this manner, optical properties in MOFs can be controlled rather easily by changing the structural parameters like the pitch length Λ and diameter d of each air hole or even the material inside of the small holes. The importance of the relative hole diameter d/Λ in particular for large-mode-area MOFs can be seen in the reliance between the transmission loss and the above mentioned numerical proportion d/Λ. It was measured this dependence loss by using an optical time-domain reflectometer (OTDR) working at operation wavelength of 1310 and 1550 nm. One can see MOFs have low transmission loss when $0.48 < d/\Lambda < 0.52$ as it is shown in Figure 2.6 [6, 7].

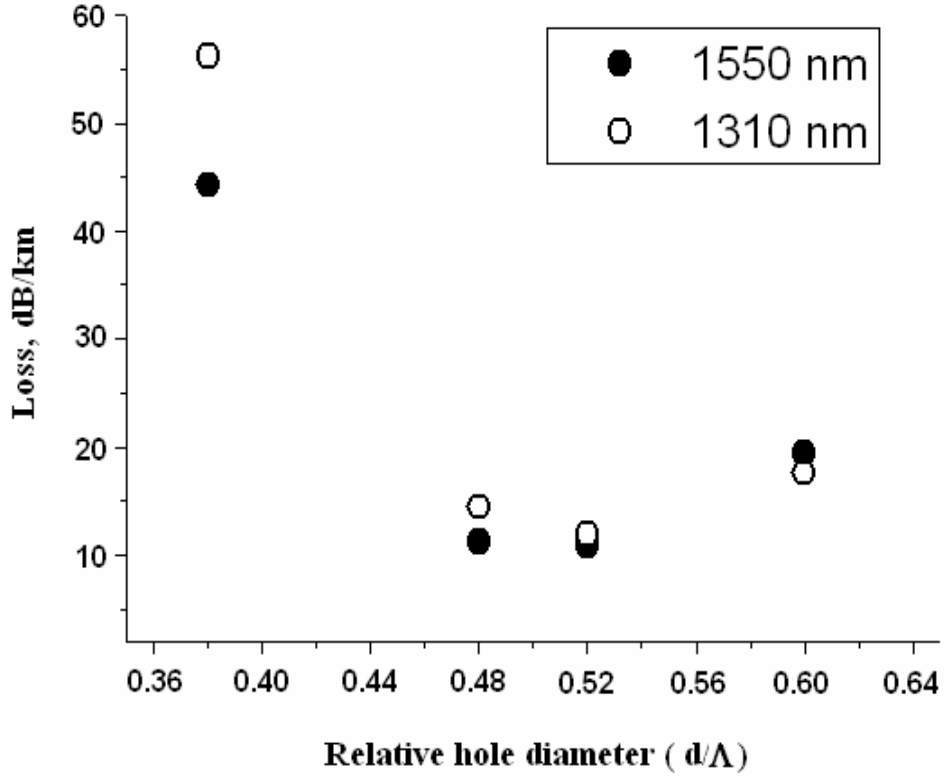

Figure 2.6 Dependence of large-mode-area MOFs transmission loss versus d/Λ measured with probe signals (OTDR) at wavelengths 1550 nm (filled circles) and 1310 nm (empty circles)

In addition, we need to remark, that pure silica refractive index $n_{Si}(\lambda)$ is a very sensitive an important parameter in the frame of theoretical and experimental operations with conventional and microstructured optical fibers (MOFs), it is for this reason that the Sellmeier formula is being applied, and its expression [9] is given by:

$$n_{Si}^2(\lambda) = 1 + \sum_{k=1}^{3} \frac{A_k \lambda^2}{\lambda^2 - B_k} \qquad (2.14)$$

where A_k and B_k stand for Sellmeier coefficients. The values for the Sellmeier coefficients of pure silica are given in the following Table 2A

	Pure Silica
A_1	0.6961663
A_2	0.4079426
A_3	0.8974794
B_1	0.0684043
B_2	0.1162414
B_3	9.8961610

Table 2A Sellmeier coefficients for pure silica

Here, we will comment a little about the production of Large-Mode-Area MOFs fibers. The method employed to fabricate LMA-MOFs fibers was based in the following procedure:

A set of identical silica capillaries were stacked into a periodic structure (see Figure 2.7), which was then fused at high temperature, in order to eliminate air gaps between the capillaries, then, this periodic structure was pulled from a composite preform, it was a silica tube containing a dense layers of thin silica capillaries, surrounding a pure silica rod. Finally, this composite-structure tube was pulled, to form microstructured optical fibers MOFs (typically LMA-MOFs have 125 μm of outer diameter and about 12 μm of core surrounded by a web of air channels).

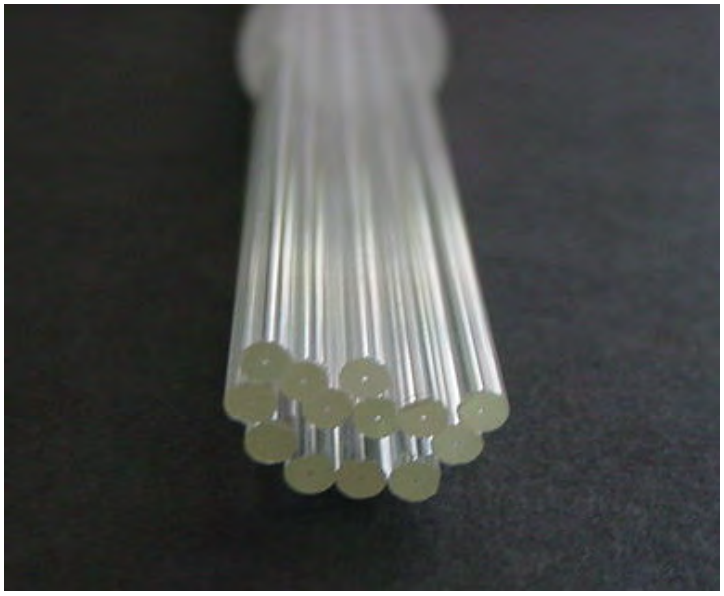

Figure 2.7 Silica thin capillaries are placed into a preform

Special precautions were taken to keep the annular shape of air holes and to eliminate the air gaps between the neighboring capillaries during the whole process. Figure 2.8 presents an end face microscope photo-image of LMA-MOF fiber with outer diameter equals to 124 μm, average air-hole diameter 2.81 μm and pitched by 5.63 μm. Figure 2.9 shows a schematic diagram of the stack-and-draw process carried out in a fire tower.

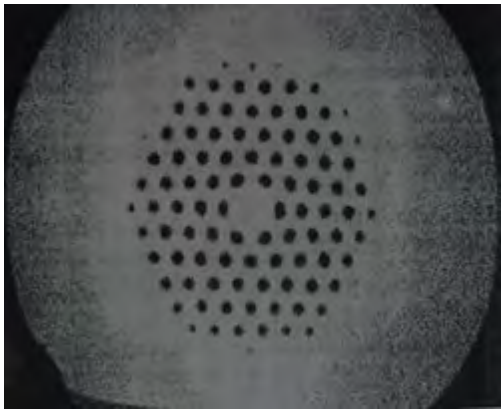

Figure 2.8 End face photo-image of a Large-Mode-Area MOF fiber of five full rings of air- holes in a hexagonal pattern.

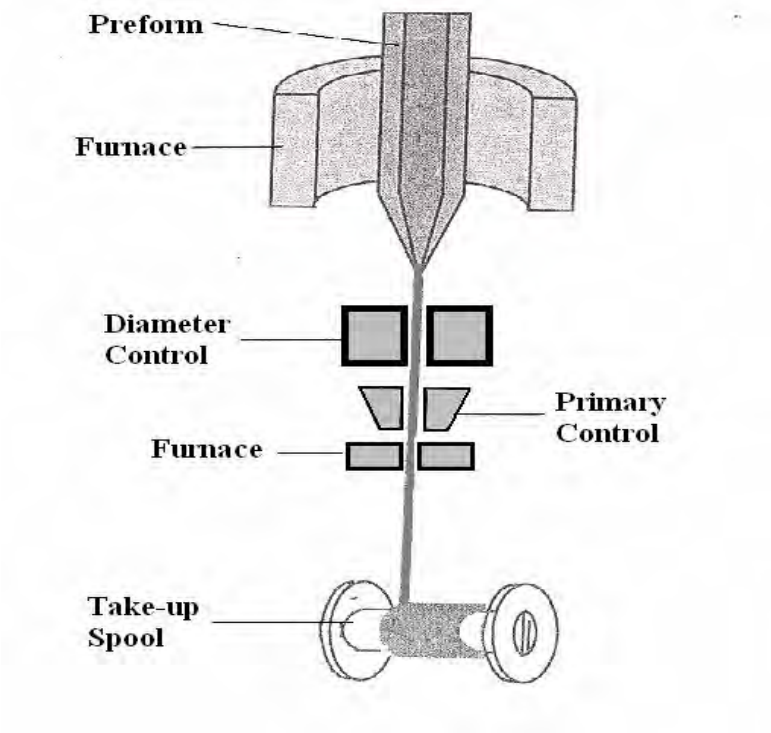

Figure 2.9 Schematic figure of drawing process of a MOF.

The principal element in the drawing of the microstructured optical fiber is the ability to preserve the highly regular structure of the preform (Figure 2.10) all the way down to fiber dimensions.

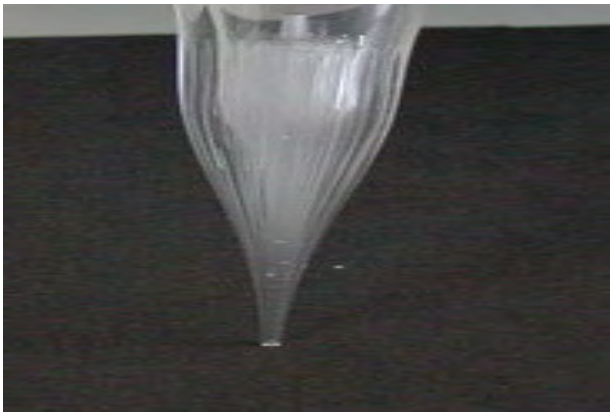

(a)

(b)

Figure 2.10 Two different preforms containing a dense package of thin silica tubes.

A conventional fiber drawn tower is shown in the following photo-image (Figure 2.11)

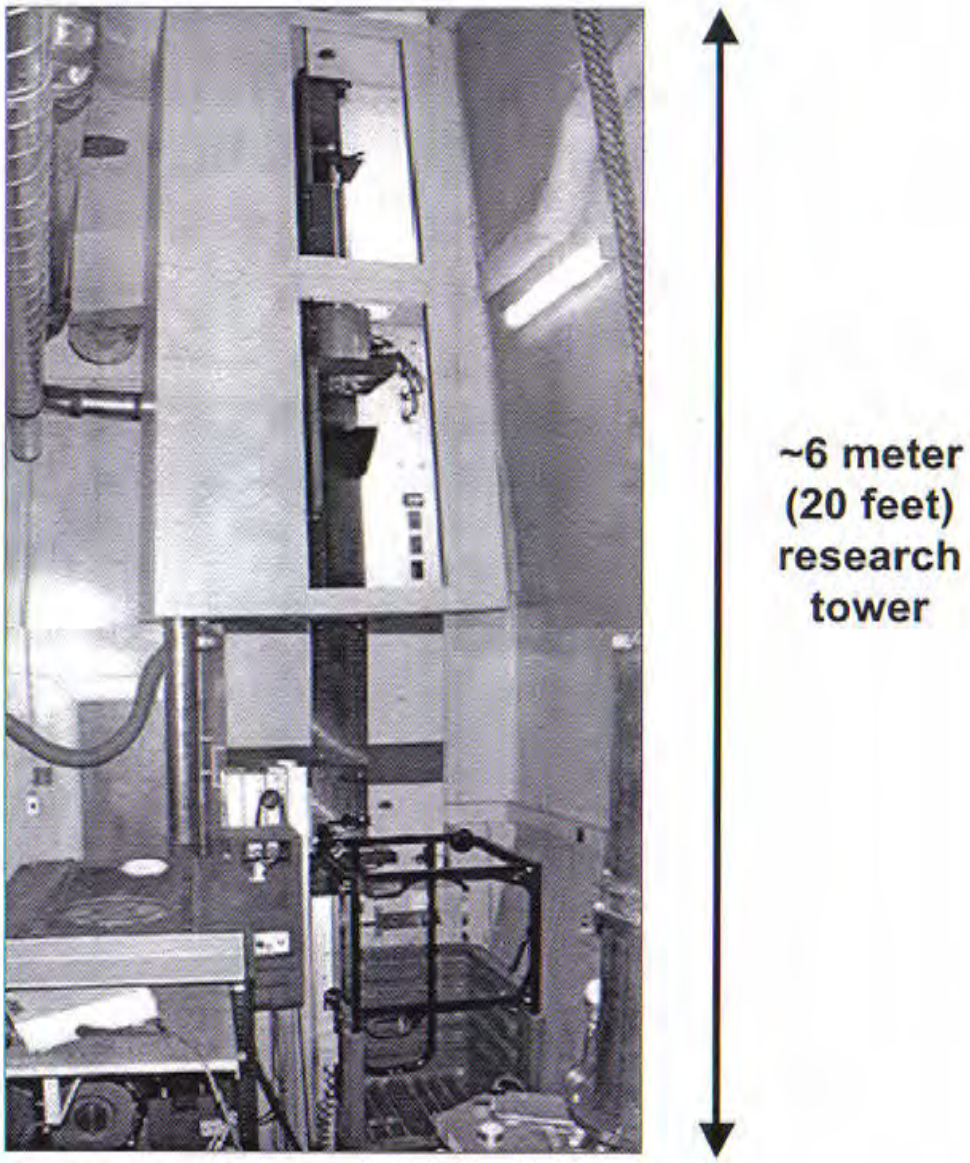

Figure -2.11 Typical fiber drawn tower for producing optical fibers.

2.5 The transport-of-intensity equation.

Recently, it has had a particular importance the work of M.R. Teague [10], where it is shown that two displaced intensity measurements should allow the gradient phase of a coherent wave to be resolved with the transport of intensity equation, expressed by:

$$k\frac{\partial}{\partial z}I = -\nabla_{\perp} \bullet \left(I\nabla_{\perp}\boldsymbol{\phi}\right) \qquad (2.15)$$

I stands for image matrix intensity, which is usually represented by a matrix of grey integer values, k; λ is the wavelength of the radiation, $\boldsymbol{\nabla}_{\perp}$ denotes the gradient operator over the plane XY, and ϕ is the phase of the bright field image.

The above transport-of-intensity equation can be understood by using the empty space time-independent wave equation (See Appendix A):

$$\left[\nabla_{\perp}^2 + \frac{\partial^2}{\partial z^2} + \left(\frac{2\pi}{\lambda}\right)^2\right]\psi_z(\vec{r}) = 0 \qquad (2.16)$$

Function ψ_z represents the plane wave traveling towards the optic axis "z" (nominal direction of radiation propagation), transverse operator $\nabla_{\perp}^2$ is taken once more for: $\frac{\partial^2}{\partial x^2} + \frac{\partial^2}{\partial y^2}$, and the k is the wavelength number.

Employing this Eq.(2.15), a knowledge of the intensity and its derivate are sufficient elements for the unique recovery of the gradient phase function, it means, the intensity derivative image can be easily obtained by acquiring experimentally the intensity in two different planes, separates by a distance Δz [11,12]

By Taylor expansion the bright field intensity may be expressed into the form:

$$I(\vec{r};\pm\Delta z) = I(\vec{r},0) \pm \Delta z \frac{\partial I(\vec{r},0)}{\partial z} + \frac{1}{2}\Delta z^2 \frac{\partial^2 I(\vec{r},0)}{\partial z^2} \pm \frac{1}{6}\Delta z^3 \frac{\partial^3 I(\vec{r},0)}{\partial z^3} \text{.....} \quad (2.17)$$

Then in the first approximation is obtained:

$$\frac{\partial I(\vec{r},0)}{\partial z} \cong \frac{I(\vec{r},+\Delta z) - I(\vec{r},-\Delta z)}{2\Delta z} \quad (2.18)$$

This above mentioned mathematical expression is placed into the intensity propagation equation (2.15), and then solved for the gradient phase $\nabla_{\perp}\phi$.

The solution of the transport of intensity equation (2.15), can be implemented using fast Fourier transforms, and the image examination method was well described in the references [13], and the method requires an in-focus image together with images defocused either side of the in-focus plane.

2.6 Defocusing image in a simple microscope system model.

We present an equivalent simple optical microscope system with laser beam as a light source that illuminates the object "*O*", lens L_1 is the objective with focal distance F_1 and L_2 is the ocular lens with focal distance F_2 separated by the distance d. A focused intensity distribution $I_{z=0}$ is produced over the plane B. Defocused bright fields images $I_{+\Delta z}$ and $I_{-\Delta z}$ are taken over planes A and C, respectively, as is shown in Figure

2.12(b). (In this case, $I_{z=0}$, $I_{+\Delta z}$ and $I_{-\Delta z}$ are representing $I(r,0)$, $I(\vec{r},+\Delta z)$ and $I(\vec{r},-\Delta z)$ respectively.

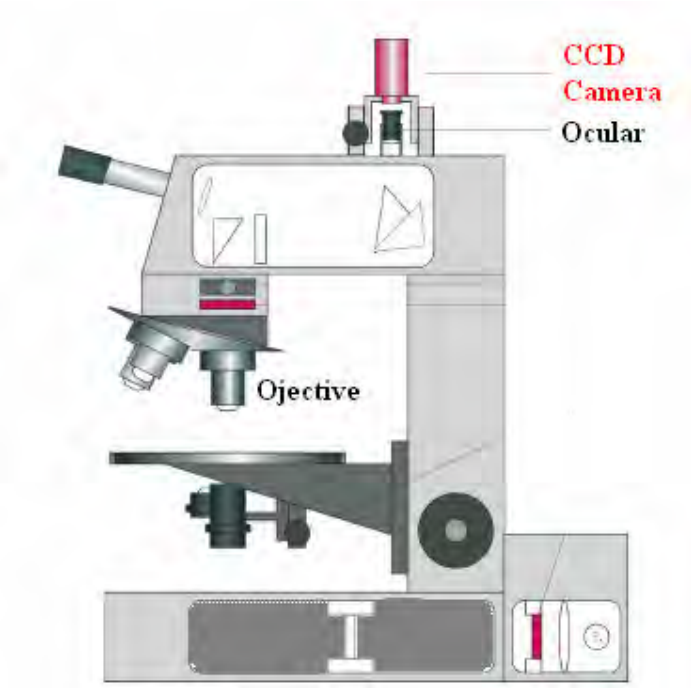

Figure 2.12 (a) Standard microscope with CCD camera

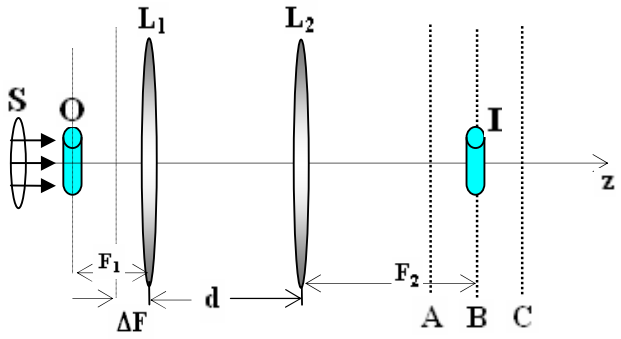

Figure 2.12(b) Scheme of an equivalent simple microscope. **S** represents the light source, ***O*** is the tested object, L_1 is the objective, L_2 is the ocular, ***I*** stands for the focused image in the plane B, and the defocused images are taken by ΔF.

The defocused bright field images $I_{+\Delta z}$ and $I_{-\Delta z}$ are obtained by moving the microscope objective by a distance ΔF with respect to the studied object.

The propagation of electric field through the previous equivalent microscope system was analyzed in Ref.14, and it was applied to study shape, size and refractive index function of biological materials. [15].

Under the condition that the tested object is illuminated by a plane wave light propagation along *"z"* direction with amplitude E_0, and by supposing that the electric field of this light after passing the phase object "*O*"[16] follows the relation:

$$E_0(\mathbf{r}) = E_0 exp(i\phi(\mathbf{r})) \tag{2.19}$$

Then, the final bright field light microscopic image in the plane B is written as:

$$I(\mathbf{r}) = I_0 + I_0 \frac{\Delta F}{k} \nabla^2 \varphi(\mathbf{r}) \tag{2.20}$$

where $I_0 \propto |E_0|^2$, $\mathbf{r} = x\hat{\mathbf{e}}_x + y\hat{\mathbf{e}}_y$, and k is the wavelength number.

A clear application of Eq. (2.20) is presented, when a refractive index function of a red cell blood (see Figure 2.13) is calculated [15].

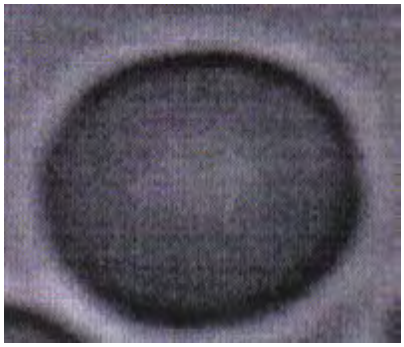

Figure 2.13 A defocused red blood cell

Therefore, it is important to notice that, the transfer of intensity equation Eq. (2.15) has similarity form with the above mentioned Eq. (2.20) (see Appendix B).

2.7 Approximation of Intensity derivative.

In the case of optical fibers, the two mentioned defocused bright field microscopic images are measured using a CCD camera system, and due to the small displacements in the dimensions of the optical fibers, bright field images are subject to the effect of experimental noises, one of them is the speckle noise, which is produced in our case by the coherent light source (laser beam).Consequently, the whole bright field intensity in the defocused planes can be calculated using a noise-free bright field image I_{Ideal} plus a noise term σ [17]:

$$\begin{aligned} I^{+}(\vec{r}) &= I^{ideal}_{+\Delta z}(\vec{r}) + \boldsymbol{\sigma}_{+\Delta z}(\vec{r}) \\ I^{-}(\vec{r}) &= I^{ideal}_{-\Delta z}(\vec{r}) + \boldsymbol{\sigma}_{-\Delta z}(\vec{r}) \end{aligned} \qquad (2.21)$$

After Taylor expansion around the zero defocus from equations (2.21), then, it is obtained the following term:

$$\frac{I^{+}(\vec{r}) - I^{-}(\vec{r})}{2\Delta z} = \frac{\partial I_{Ideal}(\vec{r},0)}{\partial z} + \frac{\Delta z^{2}}{6}\frac{\partial^{3} I_{Ideal}(\vec{r},0)}{\partial z^{3}} + \frac{\sigma_{+\Delta z} - \sigma_{-\Delta z}}{2\Delta z} \qquad (2.22)$$

The previous Eq.(2.22) has a good approach with Eq.(2.18) if it is completed that:

$$\left\| \frac{\Delta z^2}{3!} \frac{\partial^3 I_{Ideal}(\vec{r},0)}{\partial z^3} \right\| << 1 \qquad (2.23)$$

$$\left\| \frac{\sigma_{+\Delta z} - \sigma_{-\Delta z}}{2\Delta z} \right\| << 1 \qquad (2.24)$$

The assumption of small displacements for obtaining bright field microscopic images, it means that $\Delta z << 1$, then Eq. (2.23) is evidently satisfied.

On the other hand, as we have previously mentioned, when bright field images of complex objects are formed by use of the coherent light produced by a laser, a serious kind of image defect soon becomes apparent. If the tested sample is composed of surfaces that are rough on the scale of an optical wavelength, the field image is found to have a "granular" appearance. Therefore, the condition of enclosed noise into the microscopic images Eq.(2.24) can be satisfied with tools of the field of digital image processing, which generally demand extensive experimental work requiring models of simulation and testing with large sets of these sample bright field microscopic images.

References

[1] K. Okamoto, *Fundamentals Optical Waveguides,*(Academic Press, 2006).

[2] A.W. Snyder and J.D. Love, *Optical waveguide Theory,* (Kluwer Academic Press, 2000).

[3] D. Mogilevtsev, T.A. Birks, and P.St.J. Russell, "Group velocity dispersion in photonic crystal fibers", *Opt. Lett.* Vol. 23, No. 21, pp.1662-1664 (1998).

[4] T.M. Monro, D.J. Richardson, N.G.R. Broderick, and P.J. Bennett, "Holey Optical Fibers: An efficient modal model", *IEEE Journal of Light Technology,* Vol.17, No.6, pp.1093-1101, (1999).

[5] V.P. Minkovich, A.V. Kir`yanov, A.B. Sotsky, and L.I. Sotskaya, "Large-mode-area holey fibers with a few air channels in cladding: modeling and experimental investigation of the modal properties", *J. Opt. Soc. Am. B* 21, pp 1161-1169, (2004).

[6] V.P. Minkovich, A.V. Kir`yanov, and S. Calixto, "Large-hole -large-spacing holey fibers with a few air holes: fabrication and measurements of light-delivering properties and optical losses", *Laser Phy.* Vol.14, pp 767-771 (2004).

[7] V.P. Minkovich, A.V. Kir`yanov, D. Monzon-Hdz., E. Saucedo Casas, Joel Villatoro, A.B. Sotsky, L.I. Sotskaya, "Specialized Holey Fibers as a base for fabrication of tapers with selective transmission for different sensing applications", *Proc. 18th International Conference on Optical Fiber Sensors,* Cancun, Mx. (2006)

[8] N.A. Mortensen, M.D. Nielsen, J.R. Folkenberg, A. Peterson, and H.R.Simonsen, "Improved large-mode-area endlessly single-mode photonic crystal fibers", *Opt. Letters,* Vol. 28, No.6, pp.393-395. (2003).

[9] I.H. Malitson, " Interspecimen comparison of the refractive index of fused silica", *J. Opt. Soc. Am.,* Vol. 55 (10), pp1205-1210 (1965).

[10] M.R. Teague, " Deterministic phase retrieval: a Green`s function solution". *Jour. Opt.Soc.Am.* Vol. 73, No. 11, pp.1434-1441 (1983).

[11] E.D. Barone-Nugent, A.Barty, and K.A Nugent, "Quantitative phase amplitude Microscopy I: optical microscopy", *Jour. of Microscopy,* Vol.206, Pt.3, pp.194-203 (2002).

[12] M. Soto and E. Acosta, " Improved phase imaging from intensity measurements in multiple planes", *Appl. Optics,* Vol.46, No.33, pp.7978-7981 (2007).

[13] D. Paganin and K.A.Nugent, "Non-interferometric phase imaging with partially coherent light", *Phy.Rev.Lett.* Vol. 80, pp 2586-2589 (1998).

[14] U. Agero, C.H. Monken, C. Ropert, R.T. Gazinelli, and O.N. Mesquita, "Cell surface fluctuations studied with defocusing microscopy", *Phy.Rev.E,* Vol.67,

051904 (2003).

[15] L.G. Mesquita,U. Agero, and O.N. Mesquita," Defocusing microscopy: An approach for red blood cell optics.

[16] Max Born and Emil Wolf, *Principles of Optics,* 7th Ed.(Pergamon Press, 1999)

[17] D. Paganin, A. Barty, P.J. McMahon, and K.A. Nugent, "Quantitative phase-amplitude microscopy. III. The effect of noise", *Journ. of Microscopy,* Vol.214, Pt.1, pp.51-61 (2004).

Chapter 3

Refractive index function of conventional axially symmetric optical fibers.

It is well known, the refractive index profile plays a very important role in the field of optical fibers, because trough this function can be given direction to get basic properties of the optical fiber, such as mode field profiles, multimode or single-mode regimes of transmission, power attenuation coefficients, etc., etc.

3.1 Introduction.

In recent past, a new robust, rapid and non-destructive technique for calculate the refractive index profile of axially symmetric optical fibers has been developed [1]. This method is based on quantitative phase microscopy (QPM), which is sufficient to obtain

the transversal gradient of the phase $\nabla_{\perp}\phi$,from bright field microscopic images (one in focus and the others with a defocus), to which the inverse Abel transform [2,3] is used in order to get the refractive index function *n*(r).

$$n(r) = -\frac{\lambda}{2\pi}\int_{r}^{R}\frac{\nabla_{\perp}\phi\big|_{x}}{(x^2 - r^2)^{1/2}}dx \qquad (3.1)$$

R is the outer radius of the fiber and *r* is the separation from the symmetric axis of the fiber (Figure 3.1).

The term $\nabla_{\perp}\phi\big|_{x}$ represents the *x*-transverse phase gradient component.

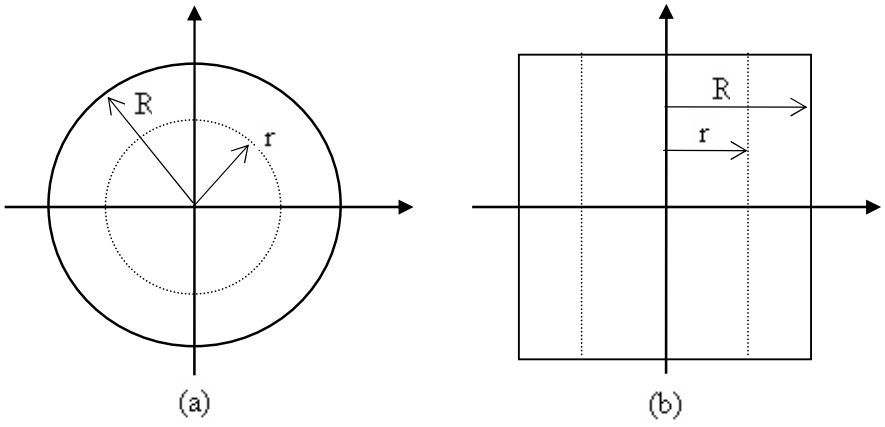

Figure 3.1 Schematic diagram showing (a) end view of the fiber and (b) transverse view.

The previous figure exhibits the end face and a transverse diagram of an axially symmetric optical fiber of a radius *R*. And in a precise way, the transverse diagram indicates the surface where bright field microscopic images are extracted.

In this reference frame, the *y* coordinate runs along the symmetric axis of the fiber, the *x* axis shows the transverse coordinate and the *z* direction gives the orientation of focus and defocus microscopic images.

As it is above mentioned in the Chapter 2, to determine the transverse phase gradient, the transport of intensity equation (2.15) is employed [4], where the involved variables are: ***I*** the intensity of the optical field measured on a transverse plane *z*, λ is the wavelength and besides *z* gives the direction of focus and defocus microscopic bright field images.

Then, to solve (2.15) for the transverse gradient phase, the Fourier transform method [5,6] can be implemented, giving the mathematical expression:

$$\bar{\nabla}_{\perp}\phi = \frac{-2\pi i}{\lambda I}\left\{\hat{F}^{-1}\left[\frac{k_x}{k_x^2+k_y^2}\hat{F}\left(\frac{\partial I}{\partial z}\right)\right]\hat{\mathbf{e}}_x + \hat{F}^{-1}\left[\frac{k_y}{k_x^2+k_y^2}\hat{F}\left(\frac{\partial I}{\partial z}\right)\right]\hat{\mathbf{e}}_y\right\} \qquad (3.2)$$

In this case, operators $\hat{F}$ and $\hat{F}^{-1}$ correspond to Fourier and inverse Fourier transformation, respectively, and k_x and k_y denotes the variables conjugated to *x* and *y*.

In this chapter, a simple experimental technique is presented for determination of bright field microscopic images that are used for the measurement of the refractive index profiles of axially symmetric optical fibers. In contrast to the Ref. 1, it has been used in the experimental setup a well-defined wavelength source (laser). Under this condition, more accuracy in the wavelength value is obtained. But contrarily, noise was increased into the bright field microscopic image. For that reason, advanced image processing tools were required. This way then, results of measurements are presented for conventional multimode graded and step index silica fibers, and also for a novel heavily

doped ytterbium-holmium silica fiber, which could be an interesting element for prospects fiber optical lasers.

3.2 Experimental Setup.

An incident He-Ne laser beam goes through the fiber sample (see Figure 3.2) and the rate given by $\Delta I / \Delta z$ is calculated from the experimental bright field microscopic images. Here, we mention that, bright field microscopic images of the studied fibers were obtained with a DC3-163 "National" microscope using a 20×0.40 numerical aperture objective.

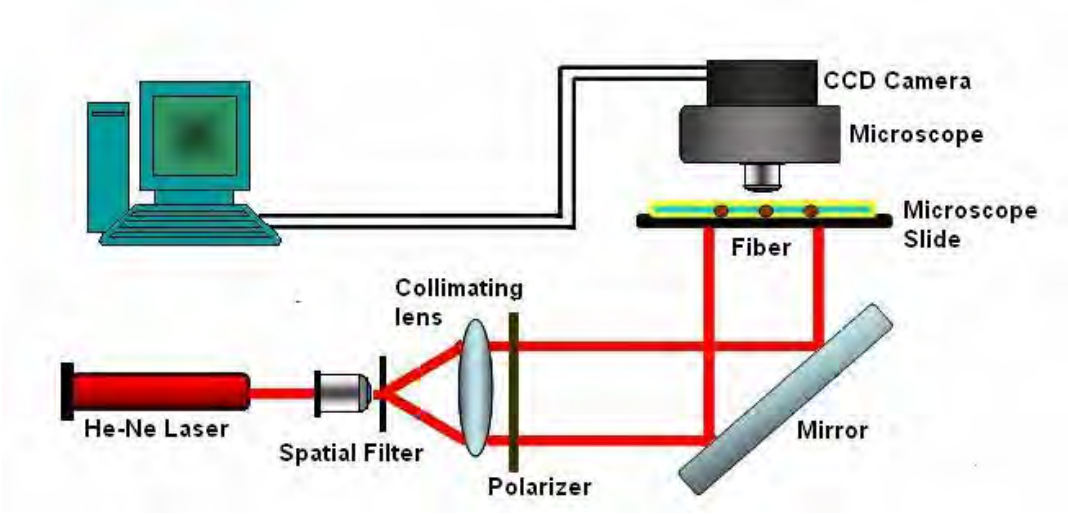

Figure 3.2 Scheme of the Experimental Setup of the optical system.

Besides a He-Ne laser, a pinhole and a collimator to obtain uniform illumination of the optical fiber are used. Using a polarizer in the experimental setup, the amount of light intensity can be regulated. An in-focus bright field microscopic images and bright field images at ± 1μm defocus were obtained with a "National" Magnaview charge-coupled

device camera with 712×582 effective pixels. The photo of the experimental setup is shown in Figure 3.3.

Figure 3.3 Experimental Setup.

With the preceding experimental setup, It has been tested a Corning 62.5/125 graded index multimode fiber, a 60/125 conventional step index multimode fiber, and a heavily doped ytterbium-holmium silica fiber fabricated in the laboratory of optical fibers [7].

As we can see in the scheme presented in Figure 3.2, a short length of each fiber without plastic coating was placed on a microscope slide. Two sections of the fibers with the same external diameter were used on each side of the fiber under study as spacers. Besides, the studied samples were also put under index matching oil before a silica cover slip was placed across the fibers (See photo in Figure 3.4).

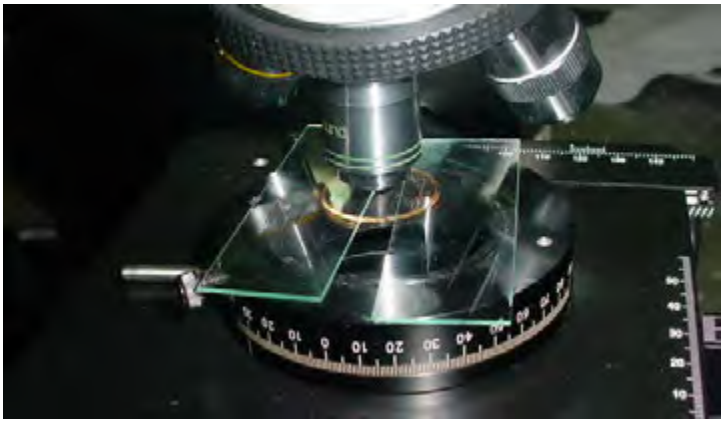

Figure 3.4 Tested optical fibers pieces are placed between silica covers.

Experimental bright field microscopic images of these studied silica fibers are presented in the following Figure 3.5.

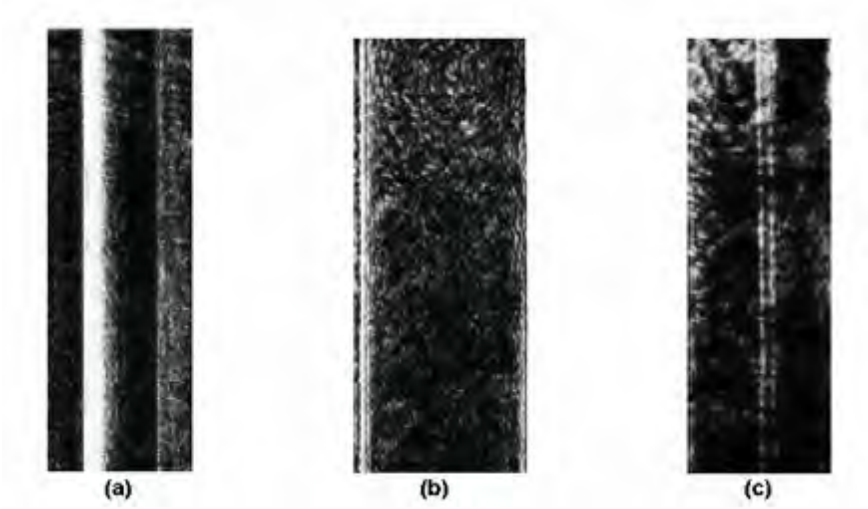

Figure 3.5 Experimental bright field microscopic image of (a) Corning 62.5/125 gradient index fiber, (b) 60/125 nearly step index fiber, and (c) doped ytterbium-holmium fiber.

3.3 Model and Results.

At first approximation we can assume that:

$$S_i(x) \approx \nabla_{\perp}\phi_i\big|_x \qquad (3.3)$$

where *i* stands for Corning 62.5/125, 60/125 step index, and experimental ytterbium-holmium silica fibers; $\phi_i(x)$ is a continuous one-variable real function, which is a symmetric function in the interval from $-R_i$ to R_i; and $\phi_i(x) = 0$ out of the interval

Then its Fourier expression can be written by:

$$\phi_i(x) = A_0^i + \sum_{k=1}^{\infty} A_k^i cos\left(\frac{k\pi x}{R_i}\right) \tag{3.4}$$

Substituting Eq.(3.3) into Eq.(3.1) for each tested optical fiber, one can obtain the relative refractive index profiles for the core of each fiber.

Figures 3.6, 3.7 and 3.8 exhibit (a) transverse phase gradient images and (b) averaged transverse phase gradient images obtained in the experiments for the Corning 62.5/125 fiber, 60/125 conventional step index fiber, and experimental, doped ytterbium-holmium silica fiber, respectively.

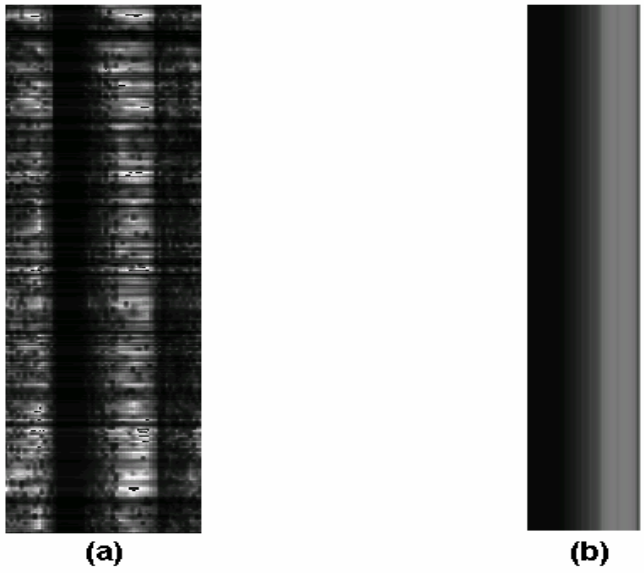

Figure 3.6 (a) Transverse phase gradient image of the Corning 62.5/125 gradient index fiber and (b) Averaged transverse phase gradient image of the optical fiber.

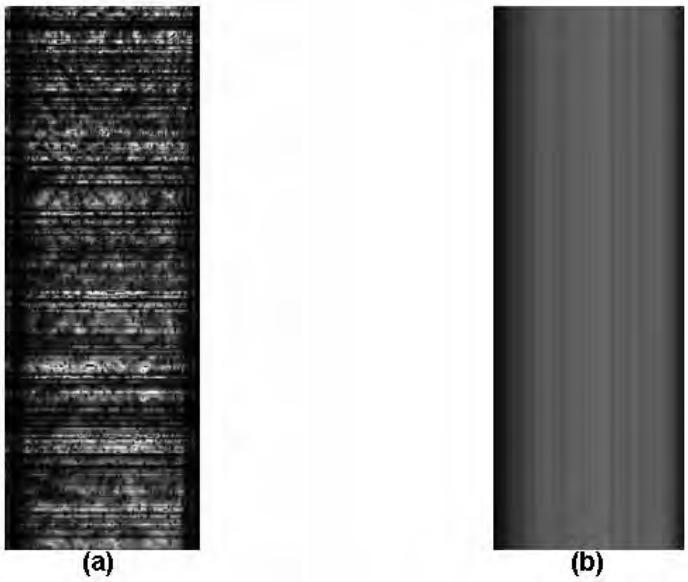

Figure 3.7 (a) Transverse phase gradient image of the 60/125 conventional step index fiber and (b) Averaged transverse phase gradient image of the optical fiber.

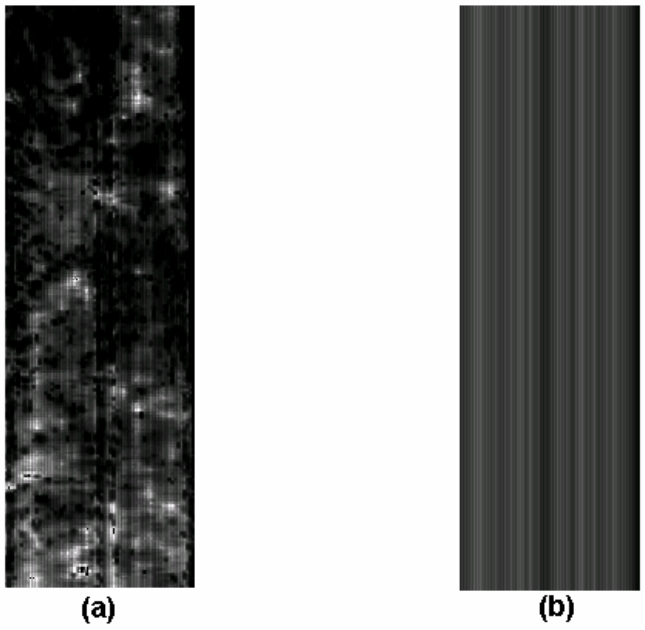

Figure 3.8 (a) Transverse phase gradient image of the heavily doped ytterbium-holmium silica fiber and (b) Averaged transverse phase gradient image of the optical fiber.

Here, we remark that in the measurements of Corning 62.5/125 optical fiber, two samples were cut from both ends of the fiber with length of 970 m. The relative index profiles step index fibers for the two tested samples for the Corning 62.5/125 is shown the following Figure 3.9.

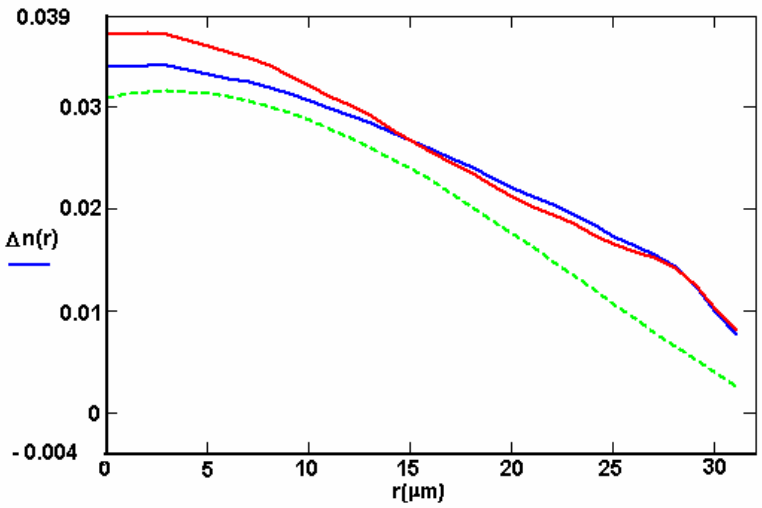

Figure 3.9 Refractive index profiles of the Corning 62.5/125 optical fiber.

The solids curves represent the refractive index profiles obtained in the experiments from the microscopic bright field image for the Corning 62.5/125 fiber using the previous transverse phase gradient method. In the precedent figure, the dashed curve is the refractive index profile obtained in the reference [1].

A comparison of these different curves shows a little discrepancy between the curves because such changes are possible for this type of the fiber [8,9]

And the refractive index profile for a 60/125 step index fiber is also shown in the Figure 3.10.

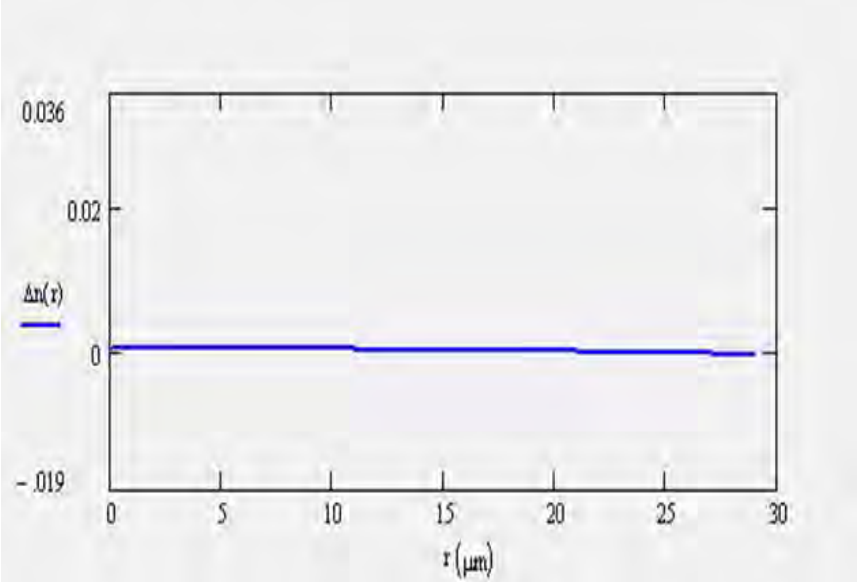

Figure 3.10 Refractive index profile of the 60/125 conventional step index optical fiber.

Finally, in the same way Figure 3.11 presents the refractive index profile for the experimental, doped ytterbium-holmium silica fiber.

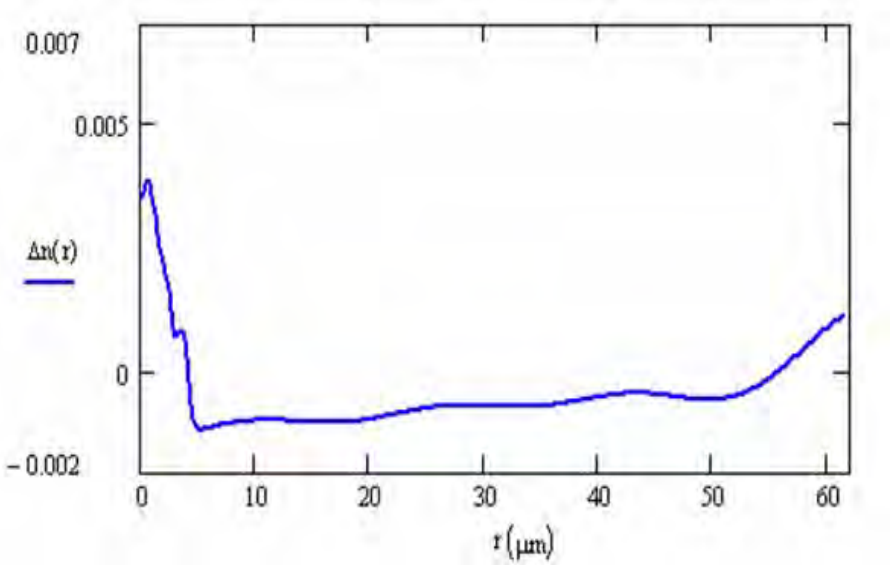

Figure 3.11 Refractive index profile of the heavily doped ytterbium-holmium silica optical fiber obtained in experiments.

3.4 Conclusions and remarks.

It has been used a simple, experimental non-destructive technique for determining of the transverse phase gradients introduced into an optical field by an optical fiber. Then these data were used to determine the refractive index profiles of an axially symmetric Corning 62.5/125, 60/125 conventional step index, and experimental, heavily doped ytterbium-holmium silica fiber. In our simple experimental setup, all bright field microscopic images were taken in a static reference frame, where all small length samples were only placed in the microscope slide, even so, many effects of noise were present. It is for this reason that, making use of the tools of statistical models for noise and imaging processing the final results were improved.

3.5 Note.

In all the measurements, it was so important the punctual source given by the spatial filter into the experimental setup. To show that, it is presented a image of a faulty pinhole and its inaccurate bright field microscopic image. As a sample, A Corning

60/125 graded index fiber is proved using again the DC3-163 Microscope with 20x0.40 NA.

Figure 3.12 Image of faulty pinhole.

Therefore, as a consequence the inaccurate bright field microscopic image is obtained. It is shown in the following Figure 3.13.

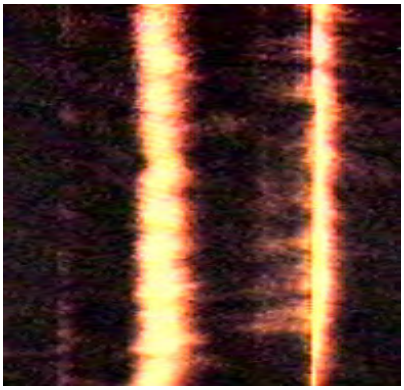

Figure 3.13 Unreliable experimental bright field microscopic image of Corning 62.5/125 graded index fiber.

References.

[1] E.Ampem-Lassen, S.T. Huntington, N.M Dragomir,K.A.Nugent, and A.Roberts, "Refractive index profiling of axially symmetric optical fibers: A new technique",

Opt. Express, Vol. 13, pp. 3277-3282 (2005).

[2] R.N. Bracewell, *The Fourier transform and its Applications* (McGraw-Hill, 2000).

[3] T. Kreis, *Holographic Interferometry* (Akademie Verlag GmbH, 1996).

[4] M.R. Teague, " Deterministic phase retrieval: a Green`s function solution". *Jour. Opt.Soc.Am.* Vol. 73, No. 11, pp.1434-1441 (1983).

[5] G.B. Arfken and H.J. Weber, *Mathematical Methods for Physicists,* (Academic Press, 1994).

[6] I.S. Gradhsteyn and I.M. Ryzhik, *Table of Integrals, Series, and Products,* (Academic Press, 1994)

[7] A.V. Kir`yanov, V.P. Minkivich, Yu. O. Barmenkov, M.A. Martinez Gamez, and A. Martinez-Rios, " Multi-wavelength visible up-converted luminescence in novel heavily doped ytterbium-holmium silica fiber under low-power IR diode pumping", *J. Lumin.* 111,pp.1-8 (2005).

[8] T. Izava and S.Sudo, *Optical Fibers:Materials and fabrications,* KTK Scientific Publishers, (1987).

[9] K. Okamoto, T. Edahiro, and M. Nakahara, "Transmission characteristics of VAD multimode optical fibers", *Appl. Opt.* 20, pp. 2314-2318 (1985).

Chapter 4

A bright field microscopic image technique for measurement of averaged index profiles of quasi-axially symmetric large-mode–area microstructured optical fiber.

It was inspected MOFs with a solid silica core surrounded by cladding, which consists of a system of air channels in silica, running along the fiber in a hexagonal structure around the core. In this case, it has been used the transverse gradient of the phase, which was obtained from bright field microscopic images of quasi-axially symmetric MOFs.

4.1 Introduction.

The refractive index profile of MOFs, as well as for conventional fibers, is again a very important property, and as we have mentioned in the chapter 3, this characteristic determines fundamental features of the MOFs.

In spite of the fact that there are only a few theoretical methods for calculation of the average index profiles for MOFs with a ideal and a simple structured of microstructured cladding [1], experimental techniques for measuring real MOFs are absent until this time. In the present chapter, we investigated large-mode-area all silica MOFs [2,3], whose cross section is a web of a few hexagonal rings of air holes with average diameter *d* and pitched by the distance Λ, see Figure 4.1. Also, it has been investigated an experimental double clad MOF.

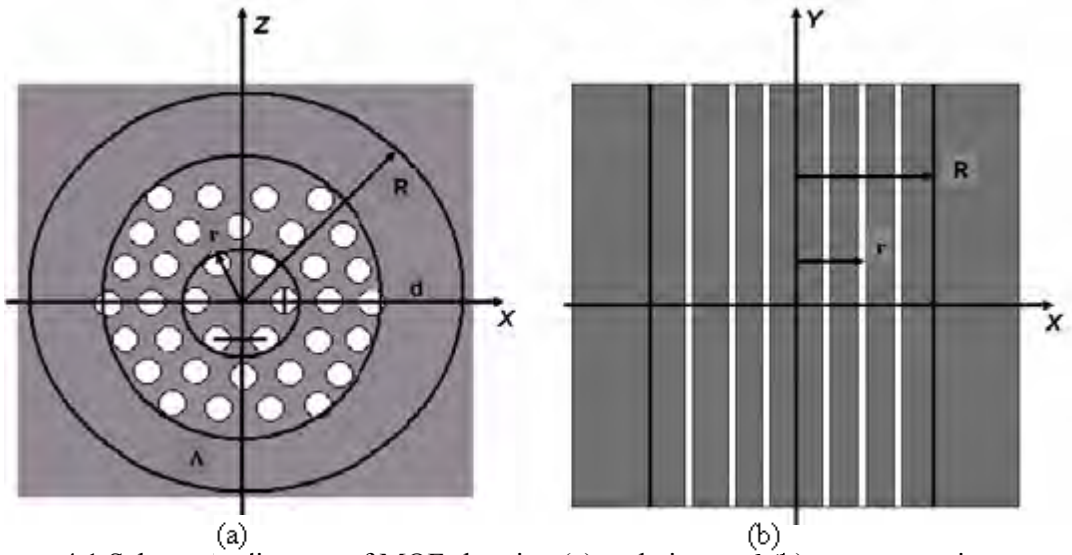

Figure 4.1 Schematic diagram of MOF showing (a) end view and (b) transverse view.

We followed the technique [4], developed for conventional fibers to obtain the transversal gradient of the phase function for MOFs from bright field microscopic images (one in focus and others with defocus ±1 μm). And with the same steps used in the previous chapter 3, the inverse Abel transform [5,6] Eq. (3.1) is here applied once more, with unchanged meaning of the transverse phase gradient $\nabla_{\perp}\phi\big|_{x}$ and the

wavelength of the used He-Ne laser (λ=632.8 nm). For our studied MOFs, the axis *y* coincides with symmetric axis of the fiber, the transverse coordinate is given by the *x* axis and the optical axis is as previously indicated by the *z* axis, where focus and defocus images are obtained. Besides, *R* indicates the outer radius of the MOF and *r* corresponds to the distance from the axis to the fiber (see figure 4.1).

The transverse phase gradient is obtained using the transport of intensity equation [7] Eq.(2.15) with the experimental bright field microscopic image ***I*** measured on a transversal plane *z*. As it has been written, the solution of the transport of intensity equation for the transverse gradient phase $\nabla_{\perp}\phi\big|_{x}$ can be calculated applying the Fourier transform method [8,9] Eq.(3.2) where Fourier operators $\hat{F}$ and $\hat{F}^{-1}$ take place again.

For the purpose of obtaining a reference frame in the qualitative measurements of the index profiles for the tested MOFs, the refractive index profile of conventional step index silica fiber was firstly measured, and additionally, due to the microscopic image noise, some image processing implements have been used [10.].

4.2 Experimental Procedure.

In the case of MOFs, bright field microscopic images were captured with a DC3 "National" Microscope using in this time two objectives in the described previous experimental setup (see Figure 3.2): one is 20x0.40 NA and the other one is 40x0.65 NA. Then, an in-focus image and images at ± 1μm defocus were obtained working with a "National" Magnaview CCD camera, with 712x582 pixels.

A short piece of each MOF sample without plastic coating was placed in a microscopic slide, where two sections of the same MOF were used similarly as spacers (see Figure 4.2).

With our experimental setup showed in Figure 3.3, we tested a conventional Corning step index fiber with 60 μm core and 125 μm cladding diameter as a reference frame.

After that, we studied an experimental MOF with two dimensional cladding with relative hole diameter $d/\Lambda = 0.42$ of the inside cladding and another large-mode-area MOF with relative hole diameter $d/\Lambda = 0.5$, both fabricated in our laboratory.

In all cases again, a short piece of each fiber without plastic coating was placed on a microscope slide, while two sections of the same fiber were used on each side of the tested fiber as spacers. The samples were also immersed into index matching oil before a silica cover slip was positioned across the fibers.

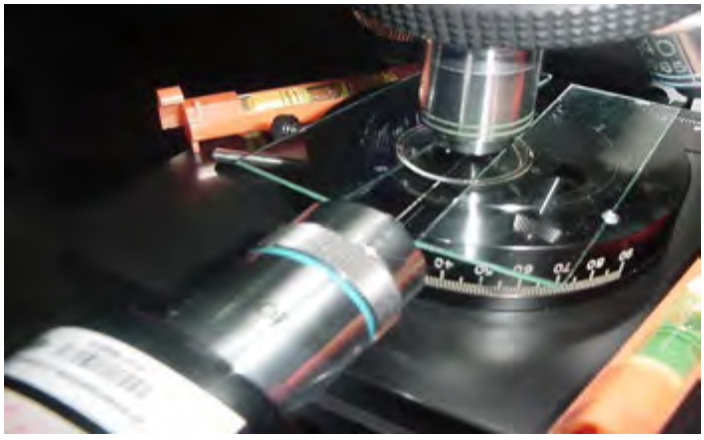

Figure 4.2 Microscope slide where the fiber pieces are placed between silica covers.

4.3 Data and Results.

Before bright field microscopic images were taken with a He-Ne laser illumination over all studied optical fibers, end face and transverse views of tested fibers were captured by CCD camera with a white microscope light (see Figure 4.3,4.6 and 4.7), as it was shown in the schematic diagram in Figure 4.1, in order to have the references frame.

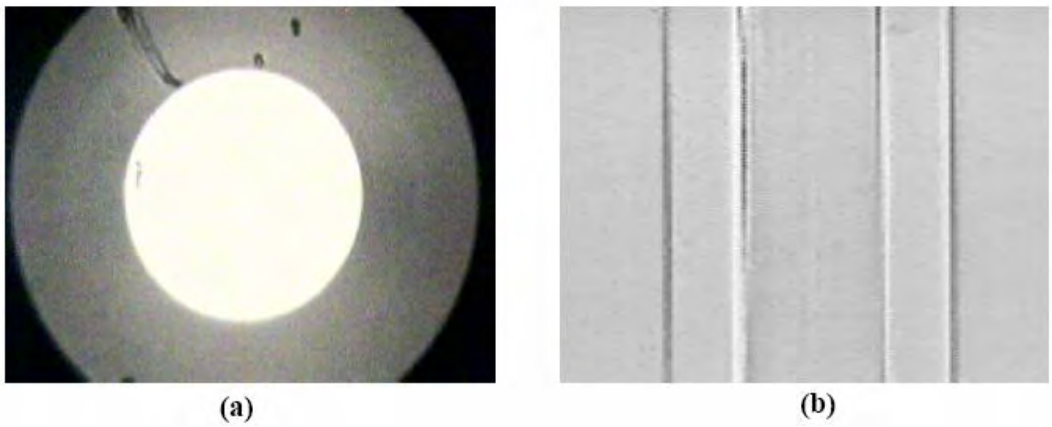

Figure 4.3 Conventional Corning 60/125 step index fiber images obtained with DC3-163 video-microscope at white light illumination: (a) end view of the fiber, (b) transverse view.

The bright field microscopic image for the reference step index fiber at its illumination with He-Ne laser, the gradient phase image and its respective average image are exhibited in Figure 4.4.

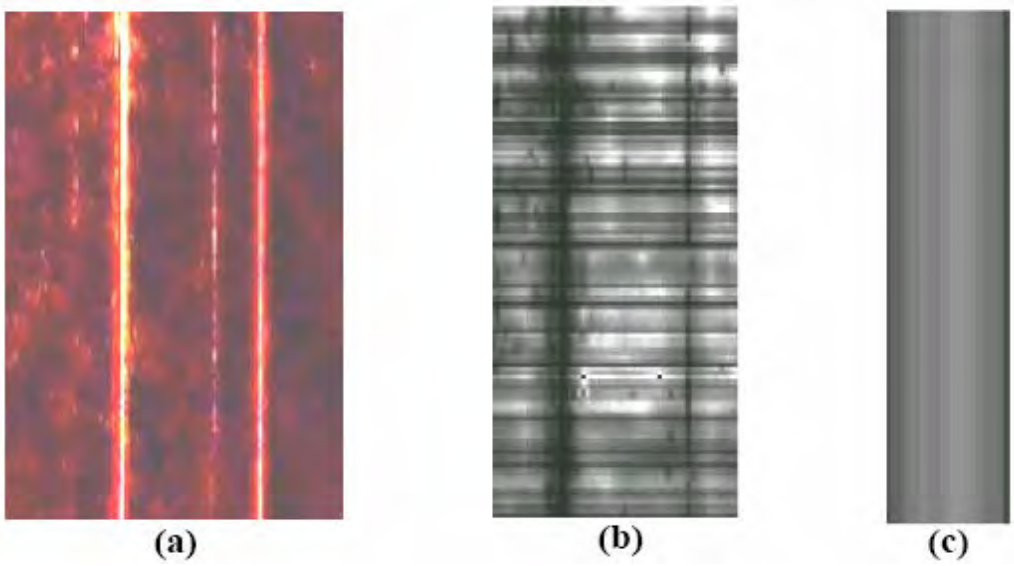

Figure 4.4 Images of Corning 60/125 step index fiber: (a) experimental bright field microscopic image, (b) transverse phase gradient image, (c) averaged transverse phase gradient image.

From the preceding average phase gradient matrix image it is possible to suppose that the transverse phase gradient can be approximate to a continuous function $S(x)$ as we have supposed in Eq.(3.3) together with the phase function ϕ, which is a symmetric function in the interval from $-R$ to R, (see Eq. (3.4)).

Substituting the continuous function $S(x)$ in the inverse Abel transform Eq.(3.1), the relative refractive index profile for the core of this conventional step index fiber was found.

Figure 4.5 shows results of our calculation. It is clear seen from Figure 4.5, that the obtained curve has a step index profile.

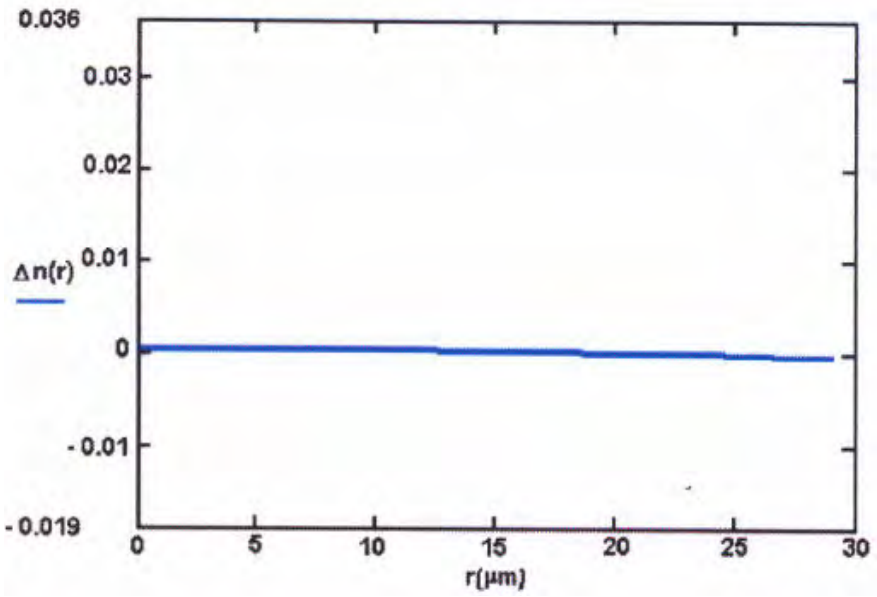

Figure 4.5 Refractive index profile of the 60/125 conventional step index fiber

For the case of the tested MOFs, images of their end and transverse view at white light illumination are shown in the following Figures 4.6 and 4.7.

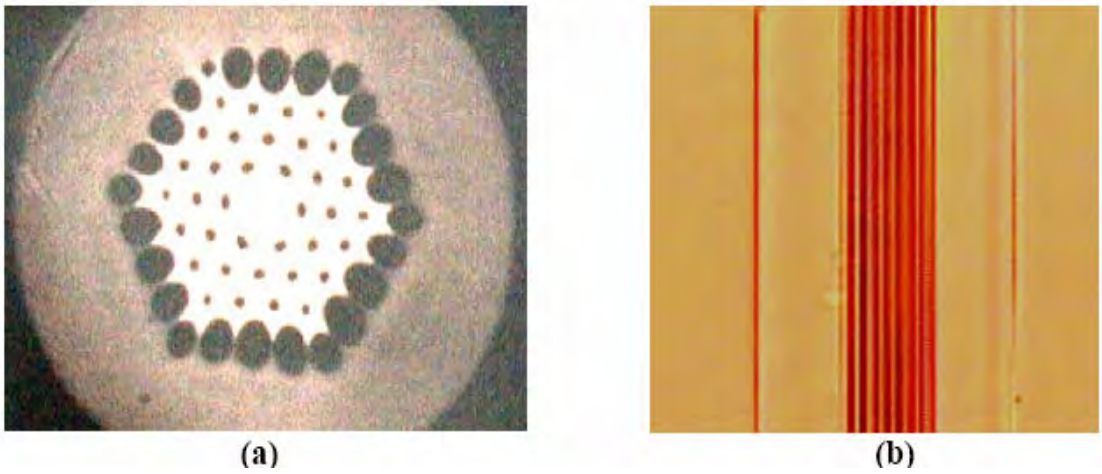

Figure 4.6 Experimental MOF with two dimensional cladding: (a) end view of the fiber, (b) transverse view. Outer diameter of the fiber is 125 μm, diameter of the core 15.6 μm, and relative hole diameter $d/\Lambda = 0.42$.

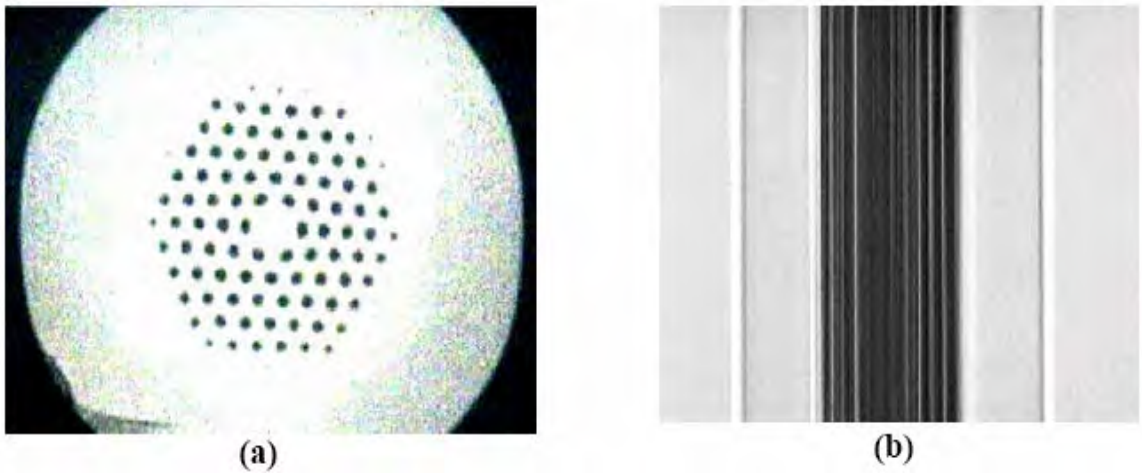

Figure 4.7 Experimental large-mode-area MOF: (a) end view of the fiber, (b) transverse view. Outer diameter of the fiber is 125 μm, diameter of the core is 11.6 μm, and the relative hole diameter of the cladding d/Λ=0.5.

Experimental bright field microscopic images of the investigated MOFs are presented in the Figure 4.8.

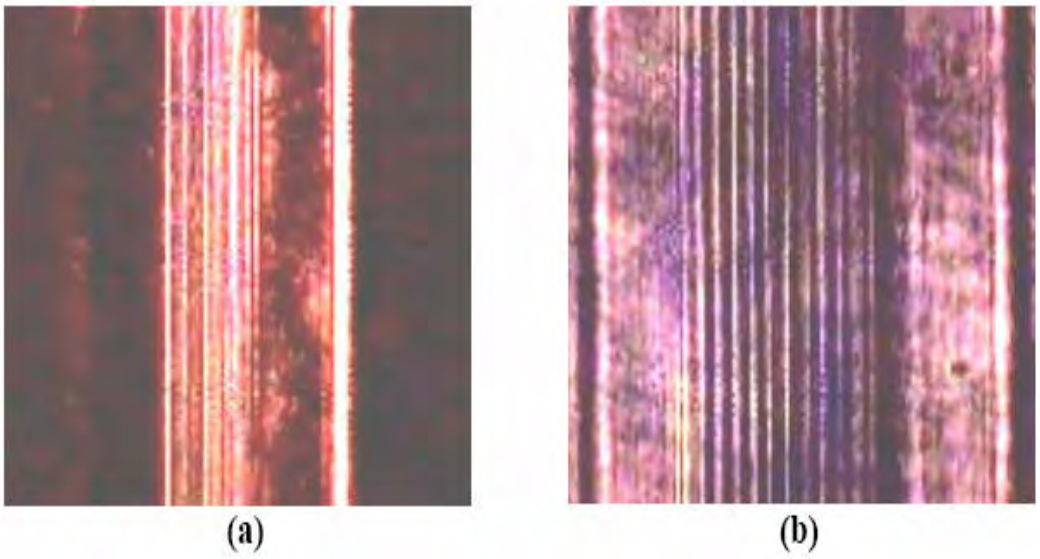

Figure 4.8 Bright field microscopic images: (a) experimental MOF with two dimensional cladding and the relative hole diameter of the inside cladding d/Λ=0.42; (b) experimental large-mode-area MOF with d/Λ=0.5.

As well as for the conventional Corning 60/125 step index fiber, the phase gradient functions for tested MOFs were obtained with the experimental setup presented in the chapter 3 (Figure 3.3), but with additional microscopic system to capture the MOFs end faces of the experimental optical fibers. (see Figure 4.9).

Figure 4.9 Experimental setup used for tested experimental MOFs.

Therefore, the phase gradient functions of the MOFs with their respective grey scale integer values can be represented (see Figure 4.10 and 4.11).

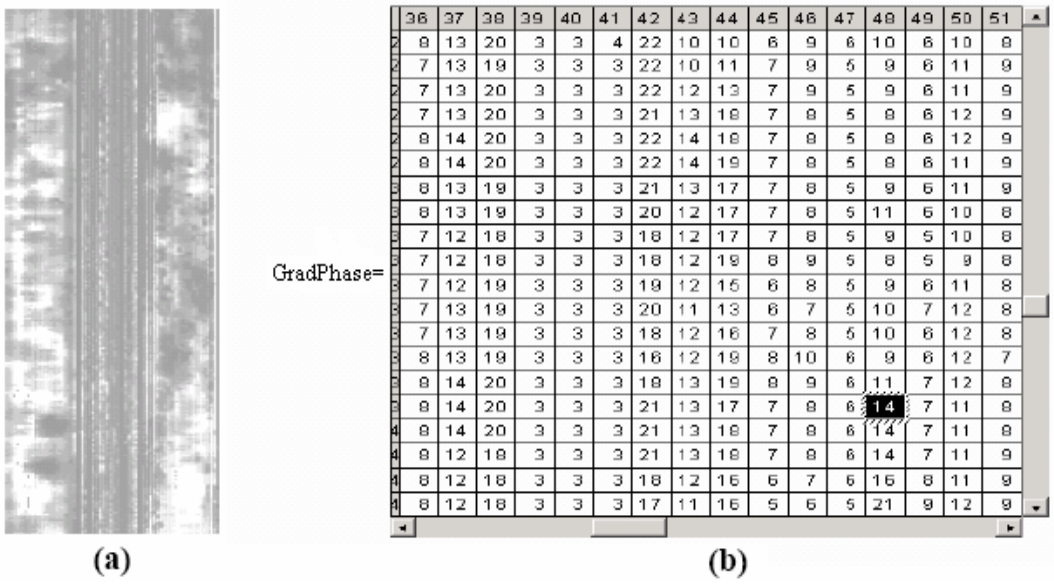

Figure 4.10 Experimental MOF with two dimensional cladding: (a) transverse phase gradient image, (b) grey scale integer values of the phase gradient image.

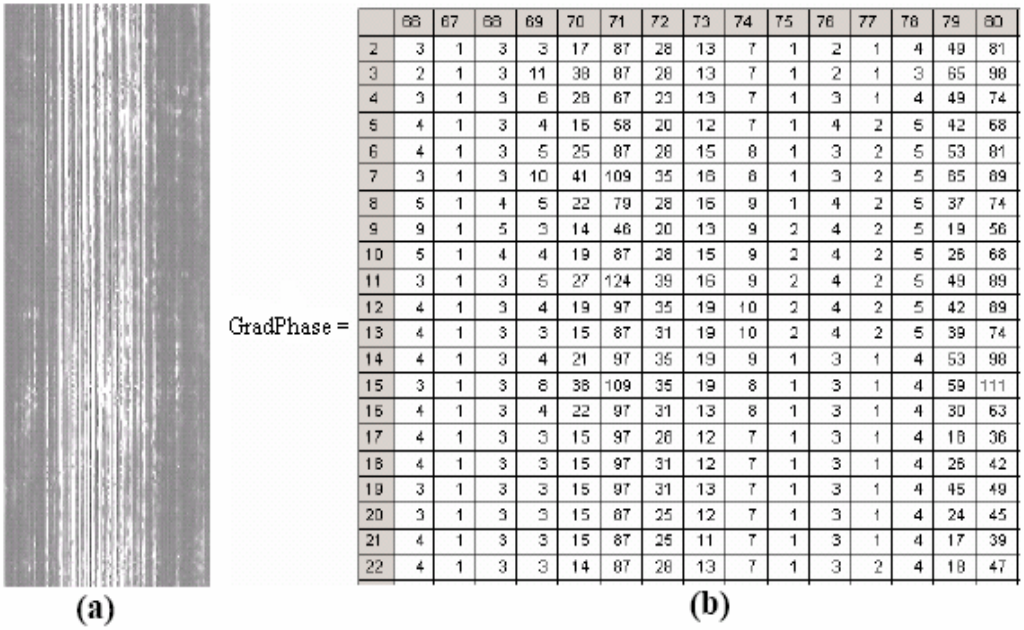

Figure 4.11 Large-mode -area MOF with d/Λ=0.5: (a) transverse phase gradient image, (b) grey scale integer values of the phase image.

Identifying the silica rings around the pure silica core inside the experimental MOFs, and using constant column values into the grey scale integer values of the phase

gradient images, after applying the above method, the following refractive index profiles of MOFs were obtained [11].

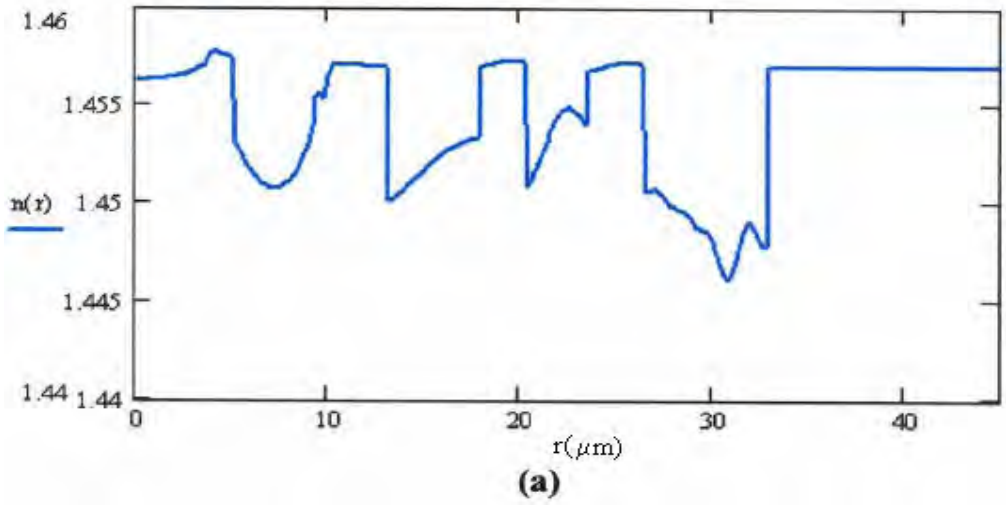

Figure 4.12 Averaged index profile for experimental MOF with two-dimensional cladding and with relative hole diameter of inside cladding d/Λ=0.42.

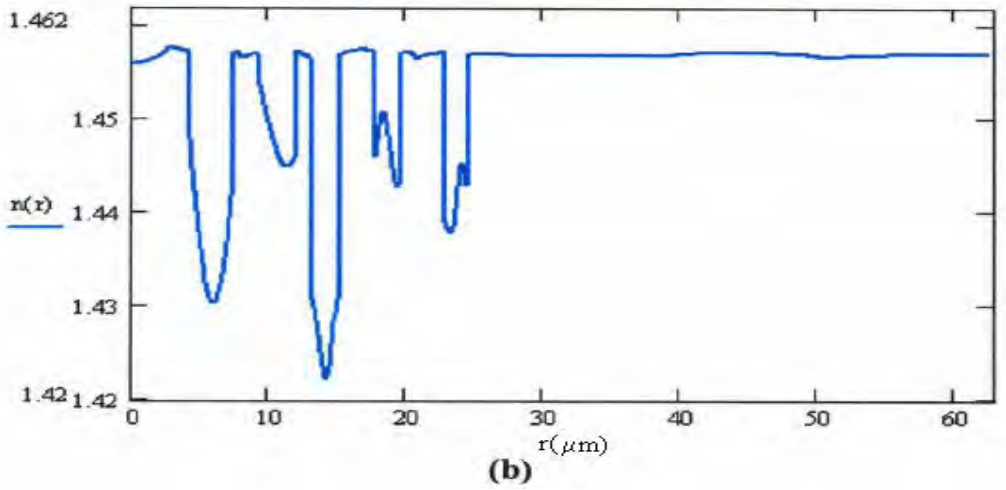

Figure 4.13 Averaged index profile for large-mode area MOF with d/Λ=0.5.

4.4 Conclusions.

To measure the average index profile of quasi-axially symmetric microstructured optical fibers (MOFs) a non-destructive and non-interferometric method has been developed.

This method is based on bright field microscopic images, which were obtained using a specially developed experimental setup.

The data of measurement for conventional Corning 60/125 step index fiber were employed as reference to get experimentally an average of a refractive index function for a fabricated large-mode-area microstructured fiber with limited number of air holes in cladding and for an experimental microstructured optical fiber with two-dimensional cladding.

References.

[1] A. Peyrilloux, S. Fevrier, J. Marcou, L Berthelot, D. Pagnoux, and P.Sansonetti, "Comparison between the finite element method, the localized function method and a novel equivalent averaged index method for modeling photonic crystal fibers", *J. Opt. A: Pure Appl. Opt.* Vol.4 pp.2331-2340 (2002).

[2] V.P. Minkovich, A.V. Kir`yanov, and S. Calixto, "Large-hole -large-spacing holey fibers with a few air holes: fabrication and measurements of light-delivering properties and optical losses", *LaserPhy.* Vol.14, pp 767-771 (2004).

[3] V.P. Minkovich, A.V. Kir`yanov, A.B. Sotsky, and L.I. Sotskaya, "Large-mode-area holey fibers with a few air channels in cladding: modeling and experimental investigation of the modal properties", *J. Opt. Soc. Am. B* 21, pp 1161-1169, (2004).

[4] E. Saucedo Casas and V.P. Minkovich, "Measurement of refractive index profiles of axially symmetric optical fibers", *Opt. Eng.* Vol. 46, 035005 (2007).

[5] R.N. Bracewell, *The Fourier transform and its Applications* (McGraw-Hill, 2000).

[6] T. Kreis, *Holographic Interferometry* (Akademie Verlag GmbH, 1996).

[7] M.R. Teague, " Deterministic phase retrieval: a Green`s function solution". *J. Opt. Soc. Am.* Vol. 73, No. 11, pp.1434-1441 (1983).

[8] G.B. Arfken and H.J. Weber, *Mathematical Methods for Physicists,* (Academic Press, 1994).

[9] I.S. Gradhsteyn and I.M. Ryzhik, *Table of Integrals, Series, and Products,* (Academic Press, 1994)

[10] E. Saucedo Casas and V.P. Minkovich, "Qualitative measurement of average index profile of symmetric microstructured optical fiber from microscopic imaging" *Proc. 19th Annual Symposium Electronic Imaging Science and Technology,* San Jose, Cal. (2007).

[11] E. Saucedo Casas, and V.P. Minkovich, "A bright field microscopic image method for measurement of averaged index profiles of quasi-axially symmetric large-mode-area microstructurd optical fibers", *16th International Laser Physics Workshop (LPHYS`07)*, León, Mx. (2007).

Chapter 5

Defocused transfer function for measurement of refractive index profiles of axially symmetric optical fibers.

It is examined in this chapter a defocused transfer function of experimental bright field microscopic images, closely connected with the evaluation of the relative index profile of the already studied axially symmetric optical fibers. It is shown that with this function, it is possible to obtain, with high precision, the defocused microscopic bright field images of investigated fibers from their focus images and, respectively, to easily evaluate the relative refractive index profiles of the fibers.

5.1 Introduction.

Recently, new simplified methods for the measurement of refractive index profiles for axially symmetric optical fibers that involve obtaining transverse images of the fibers have been developed [1,2].

Although these techniques are robust, rapid and non-destructive, they are not convenient enough when measurements of defocused images are carried out. These evaluations are tedious when done manually.

Then, the transfer function becomes a useful concept to analyze the imaging properties of a spatially invariant imaging system.

Thus, the transfer function can be used to calculate the defocused bright field microscopic images of the tested optical fibers from their respective focus bright field microscopic images.

It is well known for the defocused transfer function case that the effective pupil function $P(x,y)$ has the subsequent mathematical expression in the coordinate space [3]

$$P(x,y)=\begin{cases} exp(ikw(x,y)) & \text{if} \quad (x^2+y^2\le 1) \\ 0 & \quad\quad\quad (x^2+y^2>1) \end{cases} \tag{5.1}$$

where, $w(x,y)=C_{20}(x^2+y^2)$ is the third term (Defocus term) into the power series expansion of the general wave aberration function $W(x,y)$, C_{20} expresses the aberration coefficient for defocusing and it is usually written for a number of wavelengths $C_{20}=(\alpha/\pi)\lambda$, and k is the wavelength number. Consequently, the transfer function $g(u,v)$ for a defocused system with the above pupil function, where all other aberrations are excluded, is calculated by means of a normalized autocorrelation of the effective pupil function:

$$g(u,v)=\frac{\int_{-\infty}^{+\infty}\int P(x,y)P^*(x-u,y-v)dxdy}{\int_{-\infty}^{+\infty}\int |P(x,y)|^2 dxdy} \tag{5.2}$$

This estimation was first introduced by H.H. Hopkins.[4]

In order to get a set of bright field microscopic images of the studied fibers, a He-Ne laser source is applied for illumination of the samples. A schematic end face and a transverse representation of an axially symmetric optical fiber of radius *R* are once more shown in Figure 3.1. The transverse representation displays the plane where a bright field microscopic image is acquired.

With this reference frame, as we have described before, the *y* runs along the symmetric axis of the fiber, the *x* shows the transverse coordinate, and the *z* gives the direction of the focus and defocus images. The images in focus and with defocus [5] are needed to determine the transverse phase gradient $\nabla_{\perp}\phi$, then with the same steps specified in the preceding chapters, this function is used in the transport of intensity equation [6] Eq. (2.15), furthermore as a consequence of the reference frame in the Figure 3.1, *z* is the direction where the defocusing transfer function is being applied. Repeating the Fourier transform method [7,8] to determine the solution of the transport of intensity equation and applying the inverse Abel transform Eq.(3.1), the refractive index functions $n(r)$ together with their graphical representations of transfer functions are found for Corning 62.5/125 gradient index, 60/125 step index profile and 118/124 nearly step index profile optical fibers.

5.2 Experimental Procedure.

With the same experimental setup (Figure 3.3), the focus bright field microscopic images were taken using anew a DC3-163 “National” microscope with a 20x0.40 numerical aperture objective together with a “National” Magnaview implemented camera. A monochromatic He-Ne laser (λ=632.8 nm) was operated as homogeneous illumination over the investigated optical fibers.

Afterwards, we followed the same procedure given in the aforementioned chapter 3 for the tested optical fibers when they were placed on a microscope slide (Figure 3.4). Subsequently, focus bright field images of all above enumerated fibers are shown in Figure 5.1.

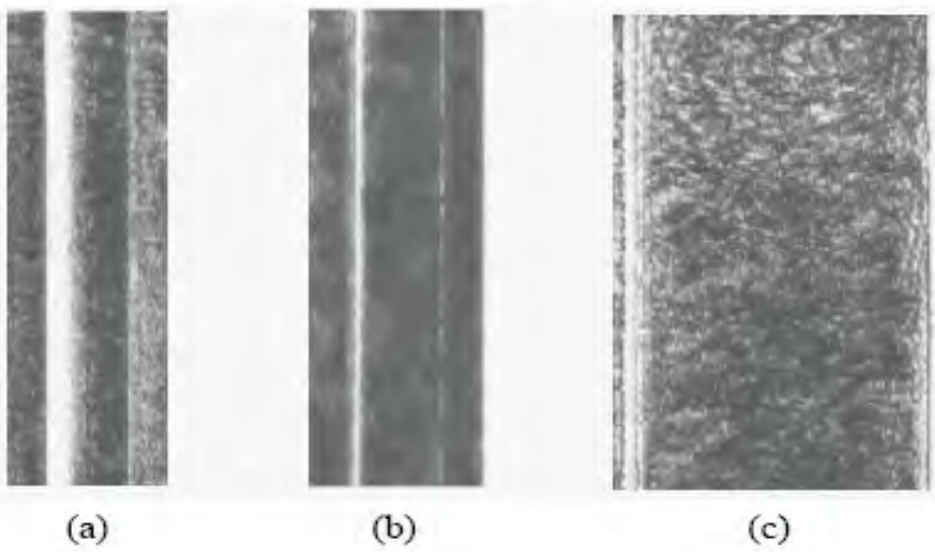

Figure 5.1 Focus bright field microscopic images of (a) Corning 62.5/125 gradient index fiber, (b) 60/125 step index fiber, and (c) 218/227 nearly step index fiber.

5.3 Analysis and Results.

Taking all our experimental microscopic fiber images into a discrete area of 512x512 pixels, then the pupil function for focal shift is written in this discrete form by:

$$P(l,m) = exp\left[2i\alpha\left((l-255)^2 + (m-255)^2\right]\right. \tag{5.3}$$

here l, m = 0,1,2……..511.

In the normalized frequency discrete space, the defocused transfer function can be calculated as the normalized autocorrelation of the of the pupil function $P(l,m)$.

Figures 5.2, 5.3 and 5.4 show (a) defocused transfer function graphs, (b) theoretical defocused bright field images in the discrete frequency domain for the Corning 62.5/125 graded index fiber, for the 60/125 step index fiber, snf for the 218/227 nearly step index fiber, respectively. Unknown parameter α has been fitted using experimental defocused

bright field microscopic images of the studied fibers, and we can notice that micrometric size of core and cladding in each studied optical fibers have a direct relation with this parameter into the pupil function $P(l,m)$ which it can be used in order to get a quality factor into the manufactured process of optical fibers.

Afterwards, following the same mathematical procedure [2] for the Corning 62.5/125 graded index fiber, for the 60/125 step index fiber, and also for the 218/227 nearly step index optical fibers, their relative index profiles can be found.

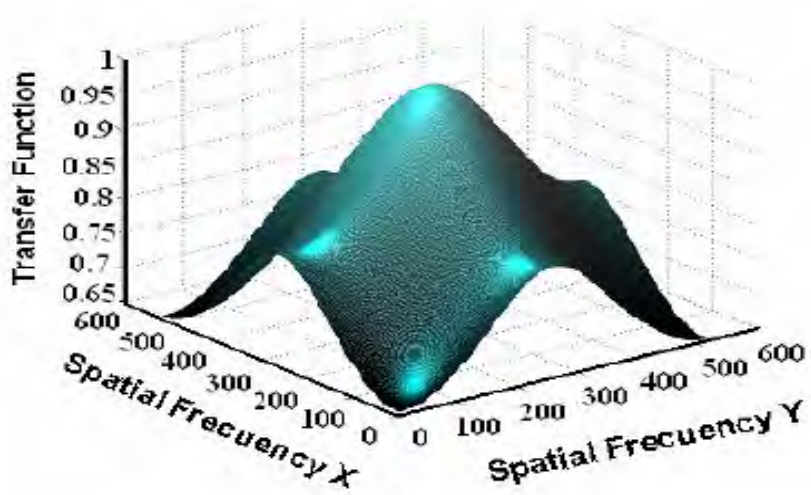

(a)

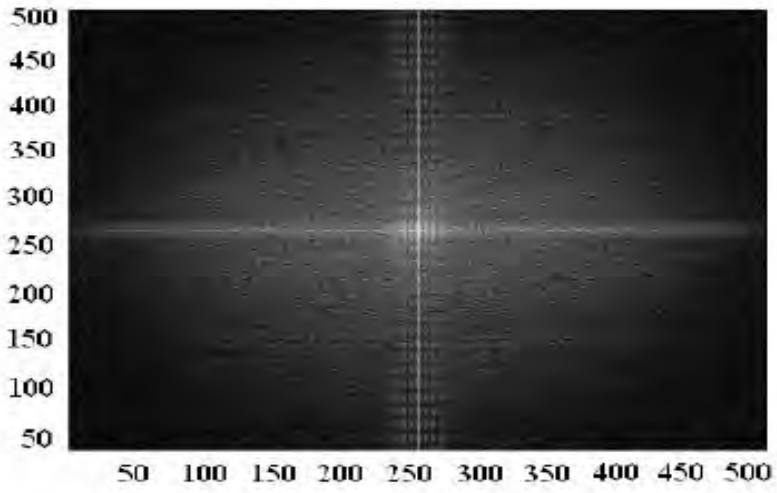

(b)

Figure 5.2 (a) Defocused transfer function of Corning 62.5/125 graded index fiber and (b) theoretical bright field microscopic image of the same fiber in the frequency domain.

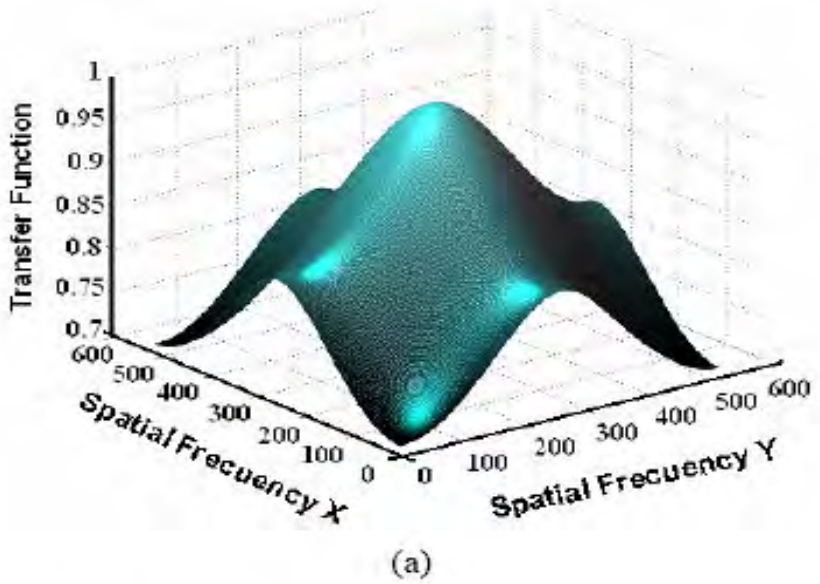

(a)

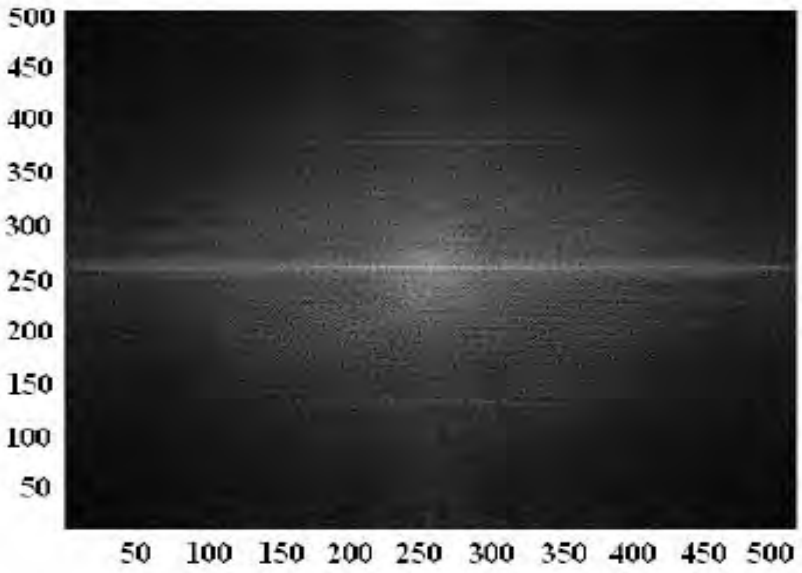

(b)

Figure 5.3 (a) Defocused transfer function of 60/125 step index fiber and (b) bright field microscopic image of the same fiber in the discrete frequency domain.

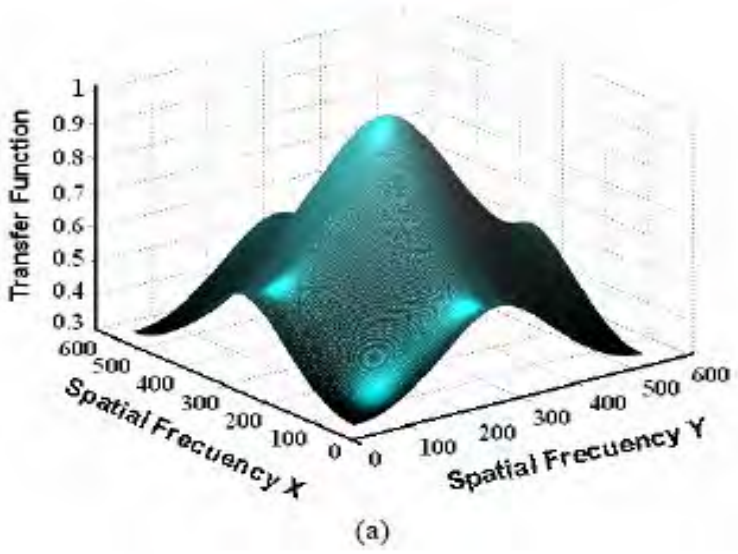

(a)

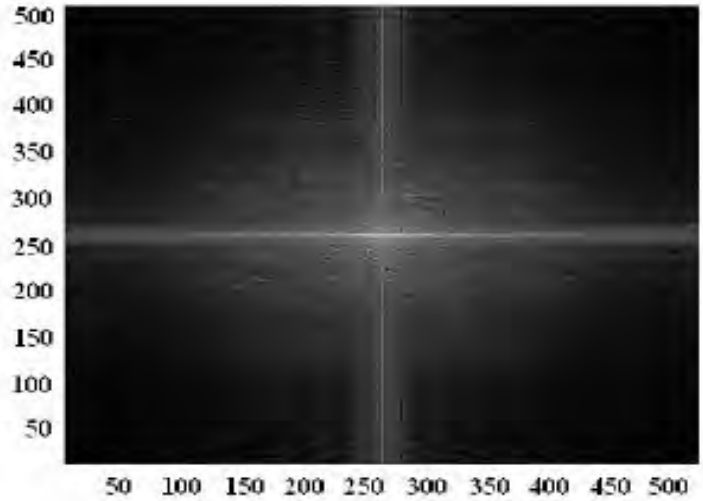

(b)

Figure 5.4 (a) Defocused transfer function of 218/227 step index fiber and (b) bright field microscopic image of the same fiber in the discrete frequency domain.

The corresponding relative index profiles are show in Figures 5.5, 5.6 and 5.7 with solid curves. Dashed curves in these figures show profiles that were registered when defocused images were done manually. One can see good agreement between the presented profiles.

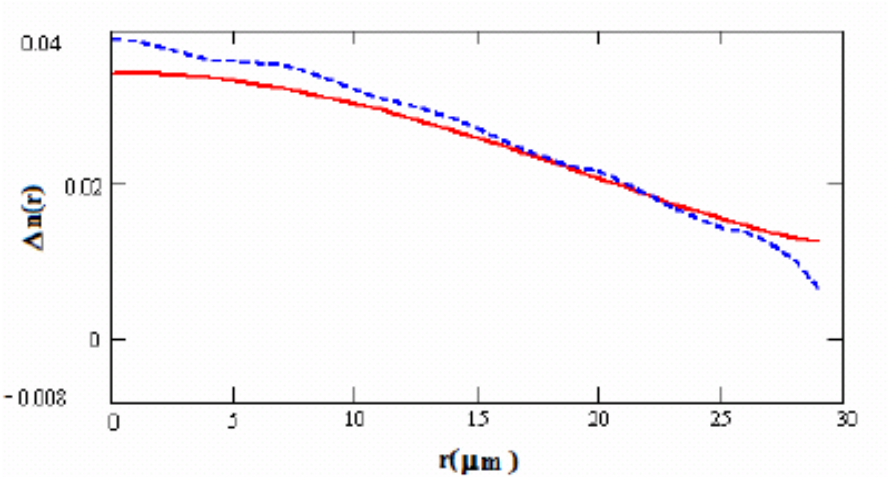

Figure 5.5 Dashed and solid curve show, respectively, the refractive index profile of the same Corning 62.5/125 graded index fiber obtained with common procedure and with the optical transfer function.

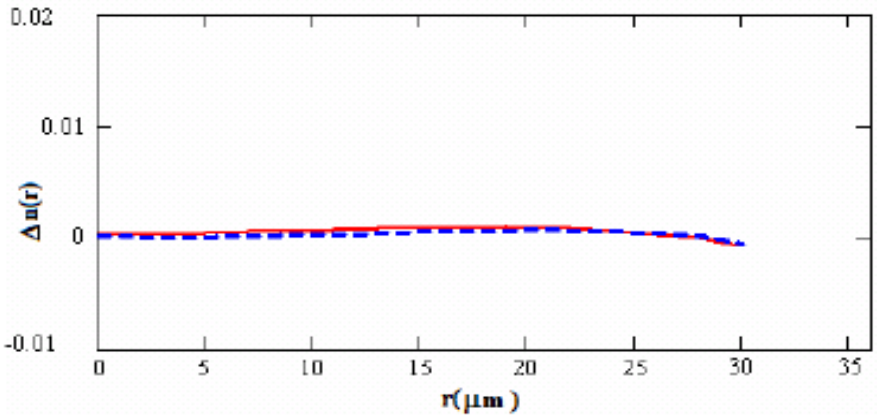

Figure 5.6 Dashed curve shows the refractive index profile of 60/125 step index fiber obtained with common procedure. Solid curve is the refractive index profile of the same fiber at using the optical transfer function.

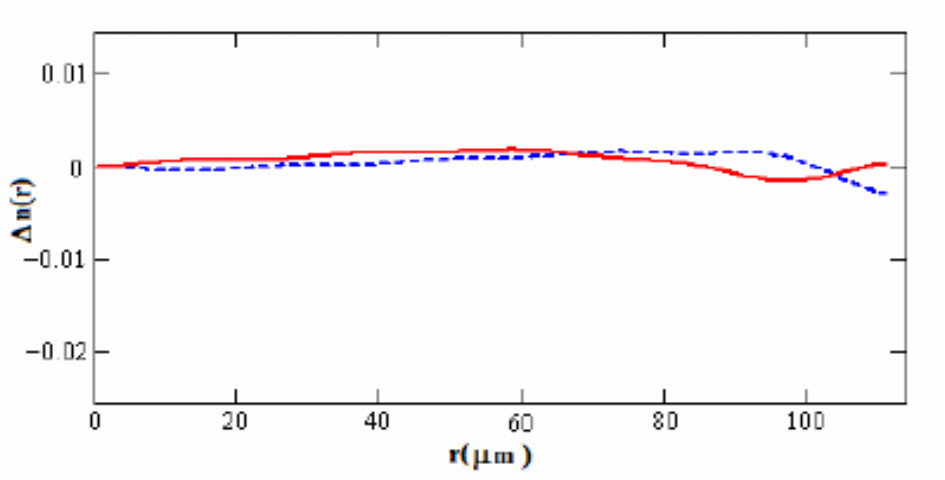

Figure 5.7 Solid and dashed curves show, respectively, the refractive index profiles of the same 218/227 nearly step index fiber obtained with common procedure and with the optical transfer function.

5.4 Conclusions.

It has been presented that defocused transfer function can provide defocused bright field images of an axially symmetric optical fiber only from its focus image. It makes possible to obtain in an easier manner the transverse phase gradient introduced into an optical field by the optical fiber. The results have been used to determine the refractive index profiles of Corning 62.5/125 graded index, 60/125 step index, and 218/227 nearly step index optical fibers.

The foregoing obtained profiles are in good agreement with the ones obtained when defocused images are prepared manually.

References

[1] E.Ampem-Lassen, S.T. Huntington, N.M Dragomir,K.A.Nugent, and A.Roberts, "Refractive index profiling of axially symmetric optical fibers: A new technique", *Opt. Express,* Vol. 13, pp. 3277-3282 (2005).

[2] E. Saucedo Casas and V.P. Minkovich, "Measurement of refractive index profiles of axially symmetric optical fibers", *Opt. Eng.* Vol. 46, 035005 (2007).

[3] C.S. Williams and O.A. Becklund, *Introduction to the Optical Transfer Function,* SPIE PRESS (2002).

[4] H.H. Hopkins, " The frequency response of defocused optical system", *Proc. R. Soc. London Ser. A* , Vol.231, pp.91-103 (1955).

[5] M Soto and E. Acosta, " Improved phase imaging from intensity measurements in multiple planes", *Appl. Optics,* Vol.46, No.33, pp.7978-7981 (2007).

[6] M.R. Teague, " Deterministic phase retrieval: a Green`s function solution". *J. Opt. Soc. Am.* Vol. 73, No. 11, pp.1434-1441 (1983).

[7] G.B. Arfken and H.J. Weber, *Mathematical Methods for Physicists,* (Academic Press, 1994).

[8] I.S. Gradhsteyn and I.M. Ryzhik, *Table of Integrals, Series, and Products,* (Academic Press, 1994)

Chapter 6

General conclusions and outlook.

It has been the purpose of this dissertation to analyze one of the principal optical characteristic (refractive index profile), as important for conventional optical fibers as for microstructured optical fibers (MOFs).In our study, multidisciplinary tools such as Fourier optics, Fourier analysis in two dimensions, Image restoration, Random process, Phase retrieval and other more have been used. In this way, a simple non-destructive and non-interferometric technique based on microscopic images was developed in order to test axially symmetric graded-index and step-index conventional optical fibers. Also this technique has been adopted for experimental investigation of an approximation for averaged index profiles of quasi-axially symmetric large-mode-area MOFs. Also a defocused transfer function of experimental microscopic bright field images, closely connected with the evaluation of the relative refractive index profile of axially symmetric conventional fibers, is analyzed. It is shown that with this function, it is possible to obtain with high precision, the defocused bright field images of the investigated fibers from their focus images and, respectively, to easily evaluate the relative index profiles of the fibers.

As a first step the method above mentioned was applied for a stationary reference system. Here the challenge starts using the same system of microscopic images for dynamics schemes

Appendix A.

The stationary wave-equation in the empty space has the subsequent expression:

$$\left[\frac{\partial^2}{\partial z^2} + \nabla_{\perp}^2 + \left(\frac{2\pi}{\lambda}\right)^2\right]\psi_z(\mathbf{r}) = 0 \qquad \text{(A1)}$$

where we used the definition $\nabla_{\perp}^{2} = \frac{\partial^2}{\partial x^2} + \frac{\partial^2}{\partial y^2}$ and the reference system is taken in

such a way that $\mathbf{r} = \mathbf{r}(x, y)$, and waves are traveling along z-direction (See Figure A).

Rewritten (A1) like product of operators:

$$L_{+}L_{-}\psi_{z}(\mathbf{r}) = 0 \qquad \text{(A2)}$$

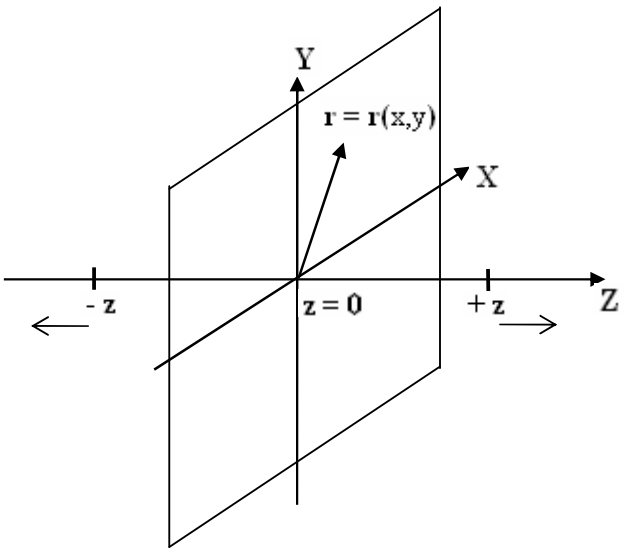

Figure A.- Reference system for a traveling wave

In the initial plane (z = 0), the wave equation may be written as:

$$\left(\frac{\partial}{\partial z} - \frac{2\pi i}{\lambda}\left(1 + \left[\frac{\lambda\nabla_{\perp}}{2\pi}\right]^2\right)^{\frac{1}{2}}\right) \bullet \left(\frac{\partial}{\partial z} + \frac{2\pi i}{\lambda}\left(1 + \left[\frac{\lambda\nabla_{\perp}}{2\pi}\right]^2\right)^{\frac{1}{2}}\right) u_{z>0}(\mathbf{r}) v_{z<0}(\mathbf{r}) = 0 \quad \text{(A3)}$$

where the wave function is defined as:

$$\psi_{z}(\mathbf{r}) = u_{z>0}(\mathbf{r}) v_{z<0}(\mathbf{r}) \qquad \text{(A4)}$$

Then, an enough condition is given by:

$$L_{+}u_{z>0}(\mathbf{r}) \bullet L_{-}v_{z<0}(\mathbf{r}) = 0 \tag{A5}$$

And, in the case, where waves travel along the $+z$ axis, we have:

$$L_{+}u_{z>0}(\mathbf{r}) = \left(\frac{\partial}{\partial z} - \frac{2\pi i}{\lambda} \left[1 + \left(\frac{\lambda \nabla_{\perp}}{2\pi} \right)^2 \right]^{1/2} \right) u_{z>0}(\mathbf{r}) = 0 \tag{A6}$$

Applying the first approach order of the square root operator, it is continued that:

$$\left(1 + \left(\frac{\lambda \nabla_{\perp}}{2\pi} \right)^2 \right)^{\frac{1}{2}} \cong 1 + \frac{1}{2} \left(\frac{\lambda \nabla_{\perp}}{2\pi} \right)^2 \tag{A7}$$

Finally, the following expression is obtained:

$$\left(i \frac{\partial}{\partial z} + \frac{\nabla_{\perp}^2}{2k} + k \right) u_z(\mathbf{r}) = 0 \tag{A8}$$

The irradiance function $I(x, y, z)$ at any point in the empty space can be written by:

$$I(x, y, z) = \left| u_z(\mathbf{r}) \right|^2 \tag{A9}$$

Then, a general wave function u_z may be described using a phase distribution:

$$u_z(\mathbf{r}) = \sqrt{I(\mathbf{r})} exp\left[i\phi(\mathbf{r}) \right] \tag{A10}$$

Multiplying Eq.(A8) on the left-hand side by u_z^* and the complex conjugate of Eq.(A8) is multiplied on the left-side by u_z. Then, if the two resulting equations are subtracted, we can obtain the *transport of intensity equation*:

$$\frac{2\pi}{\lambda} \frac{\partial}{\partial z} I = -\vec{\nabla}_{\perp} \bullet (I \vec{\nabla}_{\perp} \phi) \tag{2.15}$$

Appendix B

Taking into account the scheme of equivalent simple microscope (See Figure 2.11), the formula for the electrical field for defocused image in the plane image is given by [Physical Review E, **67**,051904 (2005)]

$$E(\mathbf{r}) = e^{i\boldsymbol{\alpha}}\left[E_0(\mathbf{r}) - i\frac{\Delta F}{2k}\nabla^2 E_0(\mathbf{r}) \right] \tag{B1}$$

where $\mathbf{r} = x\hat{\mathbf{e}}_x + y\hat{\mathbf{e}}_y$, ΔF is the out-focused distance, and k is the wavelength number.

If the tested object is illuminated by a plane wave and it alters the phase but not the amplitude, we have a *phase object* [Max Born and Emil Wolf, *Principles of Optics,* 7th Ed.(Pergamon Press, 1999)]. Then, the electric field is written as:

$$E_0(\mathbf{r}) = E_0 exp(i\phi(\mathbf{r})) \tag{B2}$$

here, $\phi(\mathbf{r})$ is the phase taken place for the illumination over the phase object. Placing the expression (B2) into (B1) we have:

$$E_0(\mathbf{r}) = E_0 e^{i\alpha} e^{i\phi(\mathbf{r})}\left(1 + i\frac{\Delta F}{2k}\left[\nabla\phi(\mathbf{r}) \bullet \nabla\phi(\mathbf{r})\right] + \frac{\Delta F}{2k}\nabla^2\phi(\mathbf{r}) \right) \tag{B3}$$

$$E_0 E_0^* = E_0^2\left\{ 1 + \frac{\Delta F}{k}\nabla^2\phi(\mathbf{r}) + \frac{(\Delta F)^2}{4k^2}(\nabla^2\phi)^2 + \frac{(\Delta F)^2}{4k^2}(\nabla\phi(\mathbf{r}) \bullet \nabla\phi(\mathbf{r}))^2 \right\} \tag{B4}$$

The first order in ΔF is used, therefore we have:

$$I(\mathbf{r}) = E_0(\mathbf{r})E_0^*(\mathbf{r}) \approx E_0^2\left[1 + \frac{\Delta F}{k}\nabla^2\phi(\mathbf{r})\right] \tag{B5}$$

The intensity of field just after passing the phase object is: $I_0 = E_0^2$, hence,

$$I(\mathbf{r}) = I_0 + I_0\frac{\Delta F}{k}\nabla^2\varphi(\mathbf{r}) \tag{B6}$$

Rewriting the previous one formulates as:

$$k\frac{I(\mathbf{r}) - I_0}{\Delta F} = I_0\nabla^2\phi(\mathbf{r}) \tag{B7}$$

In order to relate the above expression with the transfer of intensity equation (2.15), which it can be extended to:

$$-k\frac{\partial I}{\partial z} = \nabla_\perp I(\mathbf{r}) \bullet \nabla_\perp\phi(\mathbf{r}) + I(\mathbf{r})\nabla_\perp^2\phi(\mathbf{r}) \tag{B8}$$

Here, we suppose that the intensity function $I(\mathbf{r})$ is varying too slowly and the effects of phase curvature $\nabla_\perp^2\phi(\mathbf{r})$ are much bigger than this intensity derivative function, so that Eq. (B8) in the discrete space with the same defocused distance $\Delta F = \Delta z$ becomes:

$$-k\frac{I(\mathbf{r},0) - I(\mathbf{r},\Delta z)}{\Delta z} \approx I(\mathbf{r})\nabla_\perp^2\phi(\mathbf{r}) \tag{B9}$$

Finally, it is clear, that there is a close connection between Eq.(B7) and Eq. (B9).